Upper Hettangian vegetational disturbance: recovery after a mass-extinction or long-term phytotoxicity?

MSc thesis by Irene M.Waajen

Supervised by Dr. Bas van de Schootbrugge and Remco Bos

June 2020

Abstract

The Early Jurassic Hettangian stage is known as the recovery phase after the end-Triassic mass-extinction (ETE), which was one of the largest mass extinctions of the Phanerozoic era. This event occurred synchronously with volcanic emplacements from the Central Atlantic Magmatic Province, which has been implicated as the main driver of the ETE. Ecosystem stability fluctuated in the Upper Hettangian, with indications in vegetational disturbance similar to the ETE. This study aims to understand the severity of Upper Hettangian terrestrial ecosystem disturbance around the North German Basin, and to find indications for a volcanic source as a potential cause for this disturbance. A palynological study using the classification from Lindström *et al.*, 2019, revealed evidence for a heavy disturbed and toxic terrestrial ecosystem, as high abundances of mutagenic spores are found in two intervals within the Upper Hettangian, synchronous with recurrent fern spikes. In addition, high molecular weight polycyclic aromatic hydrocarbons (PAHs) were measured as a potential source of mutagenesis due to their phytotoxic properties, often associated with (volcanic) biomass burning. However, relatively low PAH concentrations are found in the intervals with increased mutagenesis, indicating a discrepancy between plant mutagenesis and PAH pollution. Although late CAMP pulses could be responsible for the Upper Hettangian aberrations, no direct link to a volcanic source can be established. An alternative explanation for the observed Upper Hettangian disturbances is astronomically driven climate forcing on the vulnerable, recovering European ecosystems. Potentially increased aridity caused soil destabilisation and erosion, while long term ozone depletion was harmful for life during periods with increased insolation. An astronomical tuning to the 405 kyr eccentricity cycle suggests a regular pacing of disturbance which ends at the base of the Sinemurian.

Contents

1 Introduction

The end-Triassic mass-extinction, ending at the Triassic-Jurassic boundary (TJB = 201.3 ± 0.2 Ma; Schaltegger *et al.*, 2008; Gradstein *et al.*, 2012; Blackburn *et al*, 2013), was the third severe extinction of the Phanerozoic era in terms of ecological impact (McGhee *et al.*, 2013; Bond & Grasby, 2017) and had long term environmental effects. The cause of the extinction is often linked to the flood basalt volcanism of the Central Atlantic Magmatic Province (CAMP), one of the most extensive Large Igneous Provinces (LIPs) on Earth (e.g. Marzoli *et al.*, 2004; Bonis & Kürschner, 2012; Blackburn *et al.*, 2013; Lindström *et al.*, 2019). The CAMP, related to the breakup of Pangea, extends over an area around the Atlantic Ocean from present South America up to Southern Europe (figure 1). The main activity of this LIP occurred likely within 1 million year, while the total global activity probably persisted from the Rhaetian to the Sinemurian (Marzoli *et al.*, 2018). Volcanic emissions released were enough to cause global environmental problems (McHone, 2003). Increased greenhouse gases such as CO_2 and CH_4 could have resulted in enhanced radiative forcing, and this increase in inorganic carbon could have enhanced ocean acidification. SO_2 aerosols could have blocked sunlight causing volcanic darkness and a decrease in photosynthesis (Beerling & Berner, 2002; Huyn & Poulsen, 2005; Van de Schootbrugge *et al.*, 2009; Whiteside *et al.*, 2010; Bond & Grasby, 2017). Toxic pollutants like polycyclic aromatic hydrocarbons (PAHs) and toxic heavy metals such as mercury (Hg) could have had teratogenic effects on terrestrial life (Nagajyoti *et al.*, 2010; Lindström *et al.*, 2019). Mercury is one of the most toxic heavy metals known to life and is persistent in the environment (Sanei *et al.*, 2012). A direct link between mercury and teratology has been made, as the timing of the Hg loading is comparable to the pulsed mutagenesis around the extinction interval (Lindström *et al.*, 2019). Mercury can cause disorders in plants by affecting its DNA causing mutagenesis (Azevedo *et al.*, 2018).

Scenarios for the end-Triassic and End Permian mass-extinctions are increasingly converging as they are both linked to the emplacement of large igneous provinces (van de Schootbrugge & Wignall, 2016). It is discussed that during the End Permian mass-extinction, released volatiles due to flood basalt volcanism could have influenced the atmosphere, leading to tropospheric transport of pollutants and a potential depletion in stratospheric ozone concentrations (van de Schootbrugge & Wignall, 2016; Bond & Grasby, 2017). Increased UV-B radiation could have affected plant reproductive systems, destabilizing the biosphere (Benca *et al.*, 2018). Due to the similarities between the extinction events, increased UV radiation might also have affected life and caused mutagenesis during the end-Triassic extinction. Malformations in sporomorphs have been observed in both extinction events, although the End Permian mass-extinction has mostly mutated pollen and the end-Triassic mass-extinction has more aberrant spores.

The Hettangian (201.5 - 199.5 Ma) is seen as the recovery phase after the end-Triassic mass-extinction event. Ecosystem recovery was unstable and in Western Europe stability did not start before the Sinemurian (van de Schootbrugge, *et al.*, 2008; van der Weijst, 2015). The causes and effects of the ETE have been studied in detail, but the recovery during Hettangian remains poorly understood. Studying the recovery phase after an extinction event is important to improve our understanding of ecosystem dynamics, which can even be used in comparison to the modern situation where we are currently dealing with a high extinction rate of species.

During the Early Hettangian, dysoxic and anoxic bottom waters were widespread over probably large regions of Northwest Europe. As sea level rose during the Hettangian, increased oxygenation lead to an increase in species diversity (Hallam, 1996). However, seas witnessed recurrent euxinia in the Early Jurassic over a period of 25 million years, peaking at the Toarchian ocean anoxic event (van de Schootbrugge & Wignall, 2016). This indicates that the end-Triassic extinction was followed by long term climatic perturbations.

Multiple cores from Northern Germany and Denmark have been studied for the Triassic-Jurassic boundary (TJB) and Hettangian recovery. A selection of what has been studied on the Schandelah-1 core is shown in figure 2. Palynological data suggests that the Late Triassic extinction interval is characterized by a high spore to pollen ratio, also known as a fern spike, linked to a disturbance in forested area. This S/P ratio varies throughout the Hettangian, indicating vegetational instability

Figure 1: The extend of the CAMP region in Pangea, where grey indicates the maximum extend and the red colour represents known basalts in outcrops or subsurface. Adapted from McHone, 2003; van de Schootbrugge *et al.*, 2009 and Whiteside *et al.*, 2010.

with multiple smaller fern spikes. The Sinemurian contains low amounts of spores without fern spikes, indicating calmer conditions with less disturbance compared to the Hettangian. Directly preceding the Triassic-Jurassic boundary, an increase in the amount of reworked palynomorphs is recorded, at the depth of the Late Triassic fern spike (figure 2). In the Upper Hettangian, at the depths of the last two fern spikes, increased reworking is observed again, although for different palynomorphs. These depths are characterized by distinctly red-coloured claystones. In addition, variations in carbon isotopes occur throughout the Hettangian, with two positive $\delta^{13}C_{org}$ excursions at the depths of two red clay beds (van de Schootbrugge *et al.*, 2018). The latest Triassic is also characterized by relatively high $\delta^{13}C_{org}$ values. Thus, multiple proxies indicate similar conditions between the extinction interval and the Upper Hettangian, although more severe in the former. As terrestrial disturbances around the ETE occur synchronously with CAMP volcanism, the question rises whether the Upper Hettangian is influenced by late pulses of CAMP volcanism.

The aim of this study is to understand the severity of stress and disturbance on the Upper Hettangian terrestrial ecosystem of Northern Germany, and to find indications for a volcanic source of this disturbance. As many proxies indicate similar conditions during the Upper Hettangian as the end-Triassic extinction, it is hypothesized that high stress levels are found in the Upper Hettangian, with evidence of volcanic interactions. Figure 2 also indicates increased concentrations of polycyclic aromatic hydrocarbons (PAHs) around the TJB, which is a proxy for burning of organic matter, here linked to CAMP volcanic activity. It is expected that increased PAH concentrations will also be found in the red claystones of the Upper Hettangian, which would indicate burning events. In this study, palynology is used to assess the vegetational variations. A focus lies on aberrant spores as this is an indication of environmental stress. In addition, polycyclic aromatic hydrocarbons are quantified to find a potential volcanic source of the environmental stress.
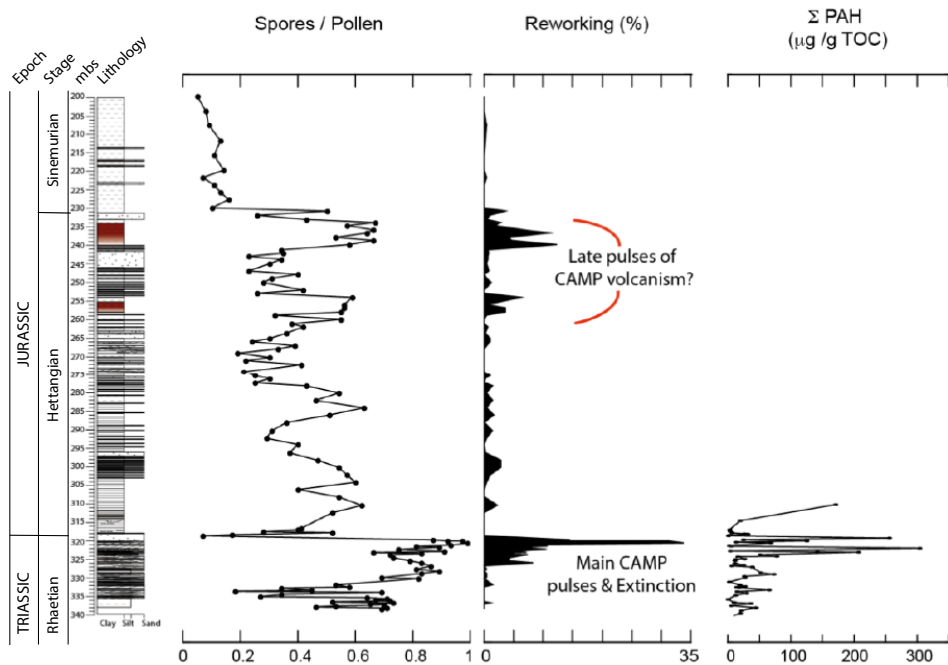
Figure 2: A selection of previous studies on the Schandelah-1 core. High amount of spores (fern spike), reworking and high PAH concentrations are found right before T-J boundary. Two red clay intervals within the Upper Hettangian also contain fern spikes and increases in reworked material (Grüters, 2012; van der Weijst, 2015; van de Schootbrugge *et al.*, unpublished data).

2 Background

2.1 Paleogeography across the Triassic-Jurassic boundary

Around the Triassic-Jurassic boundary, the supercontinent Pangea was centered close to the equator (Ruiz-Martínez *et al.*, 2012), with landmasses in the northern and southern hemisphere between 85°N and 80°S (Chandler *et al.*, 1992). Climate during the Early Jurassic was warm with high atmospheric CO_2 concentrations, a high seasonality and strong monsoons (Chandler *et al.*, 1992; McElwain, *et al.*, 1999). Model results indicate high rainfall rates over the Thetys Ocean and extreme continental aridity at low to mid latitudes of western Pangea. High seasonal temperature variations occurred mainly in high latitudes, where annual variations could have exceeded 45 °C (Chandler *et al.*, 1992). Pangea was surrounded by oceans, where sea level variations were common. In the Rhaetian a transgression occurred, with a Late Rhaetian maximum flooding surface recognised in different parts in the Northern Hemisphere (Lindström & Erlström, 2006). The spatial extent of the Late Rhaetian transgression suggests an eustatic control (Schoene, *et al.*, 2010). A following drop in sea level characterised the Triassic-Jurassic boundary (Lindström & Erlström, 2006). This regression was followed by a widespread transgression in the Hettangian (Hallam & Wignall, 1999; Hallam, 2002; Schoene *et al.*, 2010).

An epicontinental seaway was spread over Europe in the Early Jurassic, consisting of many basins (figure 3). The landmass of Pangea surrounded this sea in the south, west and north, while there was a connection to the Tethys ocean in the east. Central Europe was situated around 40°N. Sedimentation in these shallow marine basins was rather sensitive to sea level variations (Pienkowski, 2004). Climate also influences sedimentation, which could have had significant regional variations within this epicontinental seaway, from closer to the continental interior towards the margins of the Tethys Ocean (Bonis & Kurschner, 2012). In the Hettangian, the depositional environment was semi-restricted shallow marine, containing deltaic to shelf sediments. Sedimentation within the shallow epicontinental seaway was probably not constant and the occurrence of hiatuses is more than likely.
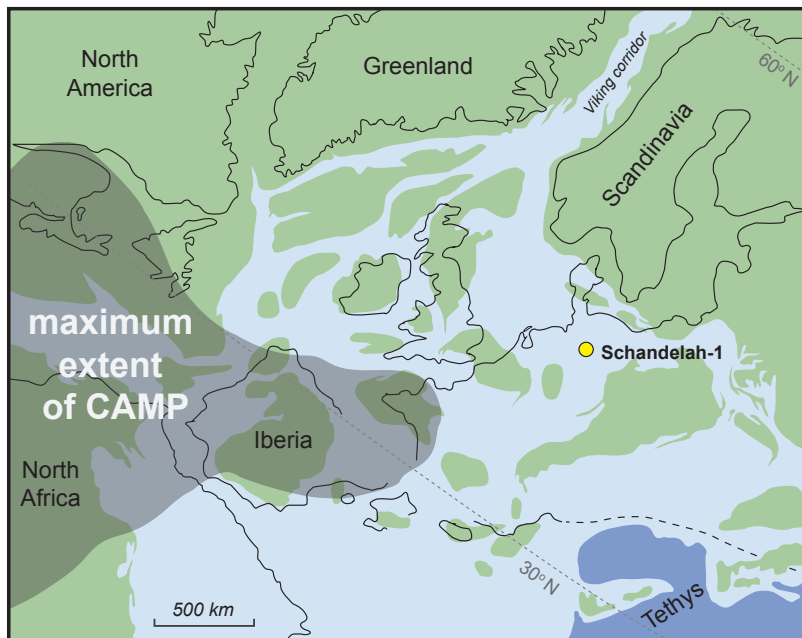

Figure 3: A paleogeographic reconstruction of Europe at 200 Ma (Hettangian), adapted from Blakey (2012). The location of the Schandelah-1 core is indicated.

2.2 Triassic-Jurassic carbon cycle

Three major negative carbon isotope excursions associated to the end-Triassic mass-extinction and pulsed CAMP volcanism have been detected in different end-Triassic successions (e.g. Heimdal *et al.*, 2018; Marzoli *et al.*, 2018). The first carbon cycle disruption is the 2 to 3‰ Marshi (or 'precursor') CIE, indicating the onset of the extinction interval (Lindström *et al.*, 2017). The second CIE is the 3 to 6‰ Spelae (or 'initial') CIE, after the first occurrence of *P. spelae*, the marker species of the start of the Jurassic, in the upper part of this CIE (Lindström *et al.*, 2017; Heimdal *et al.*, 2018). This CIE overlaps with major CAMP volcanism (van de Schootbrugge *et al.*, 2018). The 2 to 3‰ Tilmanni (or 'main') CIE is the third negative excursion, within the earliest Jurassic (Lindström *et al.*, 2017; Heimdal *et al.*, 2018). These carbon isotope excursions record major disruptions in the operation of the global carbon cycle (Beerling & Berner, 2002; Marzoli *et al.*, 2018).

During the CAMP eruptions, over 8000 Gt C as CO_2 was emitted into the atmosphere, resulting in a fourfold increase in atmospheric carbon dioxide concentration (Beerling & Berner, 2002). However, this is not enough to explain the large negative Spelae CIE. The emissions might have triggered a positive feedback loop, where the warming due to atmospheric CO_2 increase causes destabilisation of seafloor methane hydrates, emitting 5000 Gt C as CH_4 (Beerling & Berner, 2002, Heimdal *et al.*, 2018). This increase in greenhouse gases caused a rise in temperature between 2 and 6°C (McElwain *et al.*, 1999; Beerling & Berner, 2002). The excess of inorganic carbon resulted in ocean acidification, which can explain the heavy loss of reefs and the more heavily affected marine realm compared to terrestrial ecosystems. This is in line with the specific higher losses in shelly marine organisms with small buffering capacities (Bond & Grasby, 2017). Re-equilibrium of the atmosphere-ocean system was reached after 0.7 - 1.0 million years (Beerling & Berner, 2002).

The organic carbon isotope record of the Hettangian is complex and shows fluctuations throughout the Hettangian. Bartolini *et al.* (2012) present a positive excursion in carbon isotope values in the upper half of the Upper Hettangian Angulata zone (figure 4). Correlation of this positive excursion between geographically distant locations implies a hemispherical to global interpretation. In some locations it shows 2 separate positive excursions, which are also clear in the Schandelah-1 core where they coincide exactly with the two red intervals. These high $\delta\,^{13}C_{org}$ values are not present everywhere; for example, isotope values in the Mingolsheim core (Southern Germany) and Val Adrara section (Italy) are significantly low in the Angulata interval (Quan *et al.*, 2008; van de Schootbrugge *et al*, 2008).

2.3 CAMP volcanism and PAH pollution

The distribution of CAMP volcanism was sourced by deep mantle plumes, which originated from the core-mantle boundary (Ruiz-Martínez *et al.*, 2012). This volcanism was linked to a rift zone, which eventually resulted in the opening of the Atlantic Ocean and the breakup of Pangea. CAMP flood basalts initially covered an area over 2.5 million km^2, but potentially approached 10 million km^2. With a volume between 2 and 4 million km^3, CAMP is one of the largest LIPs of the Phanerozoic (Bond & Grasby, 2017). Earliest CAMP volcanism (201.635 ± 0.029 Ma) started right before the start of the end-Triassic extinction event (201.564 ± 0.015) around 250 kyr before the TJB (e.g. Marzoli *et al.*, 2011; Blackburn *et al.*, 2013; Heimdal *et al.*, 2018).

An increase of polycyclic aromatic hydrocarbons (PAHs) in the sediment can be an indication of volcanism (Murchison & Raymond, 1989). PAHs are compounds with 2 or more fused aromatic rings (Menzie *et al.*, 1992), which can be formed by incomplete combustion of organic matter by high temperatures due to wild fires, intrusive or extrusive volcanic contact metamorphism of high-organic deposits, by diagenetic alterations of biolipids or by soil erosion (figure 5; Murchison & Raymond, 1989; Menzie *et al.*, 1992; Grice *et al.*, 2007). PAHs may also originate from extraterrestrial organic matter, which would have a different carbon isotope signature than terrestrial PAHs (Naraoka *et al.*, 2000). Combustion-derived PAHs are those PAHs formed by burning (wildfires or extrusive or intrusive volcanism), and have been found in ancient sediments (Nabbefeld, *et al.*, 2010). The Permian-Triassic boundary and Triassic-Jurassic boundary, which both coincide with a major mass extinction, have been studied for
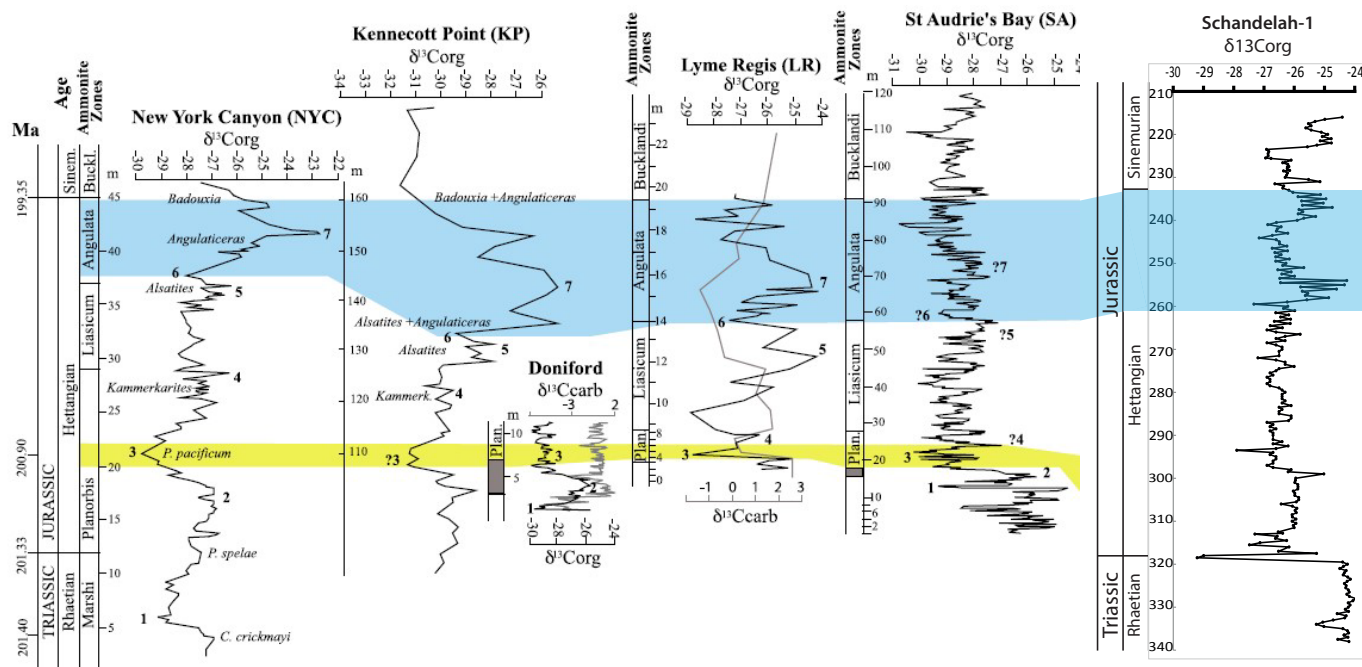
Figure 4: Organic carbon isotope records from the Late Triassic up to the Early Sinemurian from different locations (Bartolini *et al.*, 2012.), including the Schandelah-1 core (data from van de Schootbrugge *et al.*, 2018). The Angulata zone, where this study focuses on, is highlighted in blue. The extent of the Angulata zone in the Schandelah core is poorly constrained due to low ammonite abundances, making the lower boundary uncertain.

increased PAHs (e.g. Marynowski & Simoneit, 2009; Nabbefeld, *et al.*, 2010; Pienkowski *et al.*, 2011; Grüters, 2012). Combustion-derived PAHs are larger, 3 to 7-ringed, unsubstituted molecules, being pyrene, fluoranthene, benzo[a]anthracene, benzo[e]fluoranthene, benzo[k]fluoranthene, benzo[e]pyrene, benzo[a]pyrene, benzo[ghi]perylene, indeno[1,2,3-cd]pyrene and coronene (Jiang *et al.*, 1998), (plate 1). Of these, benzo[e]pyrene has been proposed to be the most stable component of all 5-ringed PAHs (Stein, 1978; Nabbefeld, *et al.*, 2010). Perylene is a 5-ringed PAH which is not linked to combustion, but is formed by depositional diagenetic alterations of biological precursors (Jiang, *et al.*, 1998) and is used as a biomarker for fungal organic matter. Chrysene is a 4-ringed PAH which can form both due to combustion or by diagenesis (Jiang, *et al.*, 1998).

Polycyclic aromatic hydrocarbons are toxic substances which can be transported long distances through the atmosphere (van de Schootbrugge, *et al.*, 2009). PAHs are known for their mutagenic, carcinogenic and toxic properties (Maliszewska-Kordybach, 1999) and may cause mutations and defoliation in terrestrial vegetation (e.g. Stein, 1978; Pienkowski *et al.*, 2012). Benzo[a]pyrene (BaP) is strongly carcinogenic and has been studied over the past century (Freeman & Cattell, 1990). Other PAHs considered as probably carcinogenic are at least benzo[a]anthracene, chrysene, benzo[b]fluoranthene, benzo[k]fluoranthene, benzo[a]pyrene, indeno[l,2,3,c-d]pyrene, dibenzo[a,h]anthracene and benzo[g,h,i]- perylene (Menzie 1992).
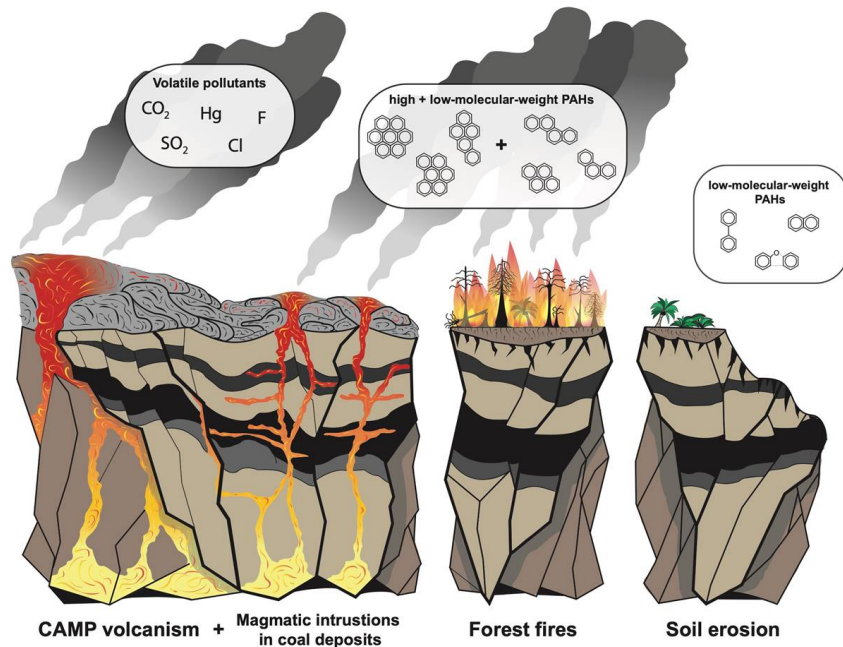
Figure 5: Volcanic pollution and different paths to the formation of PAHs: volcanic intrusions in organic rich sediments, forest fires, and soil erosion. Adapted from van de Schootbrugge & Wignall, 2016.
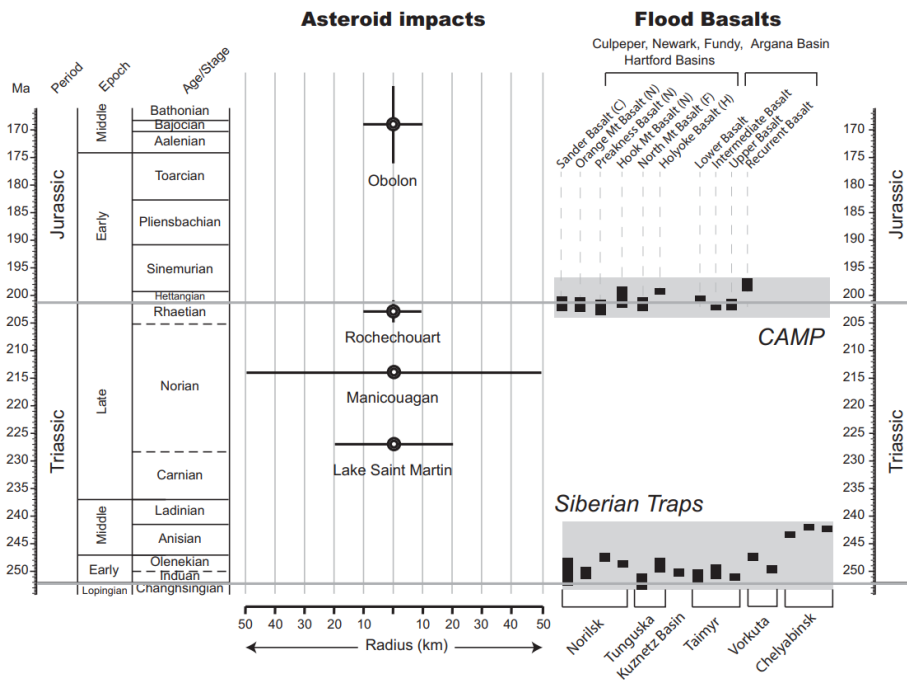
Figure 6: Timing of large scale volcanism and asteroids impacts in the Triassic and Early Jurassic. Retrieved from van de Schootbrugge & Wignall, 2016.
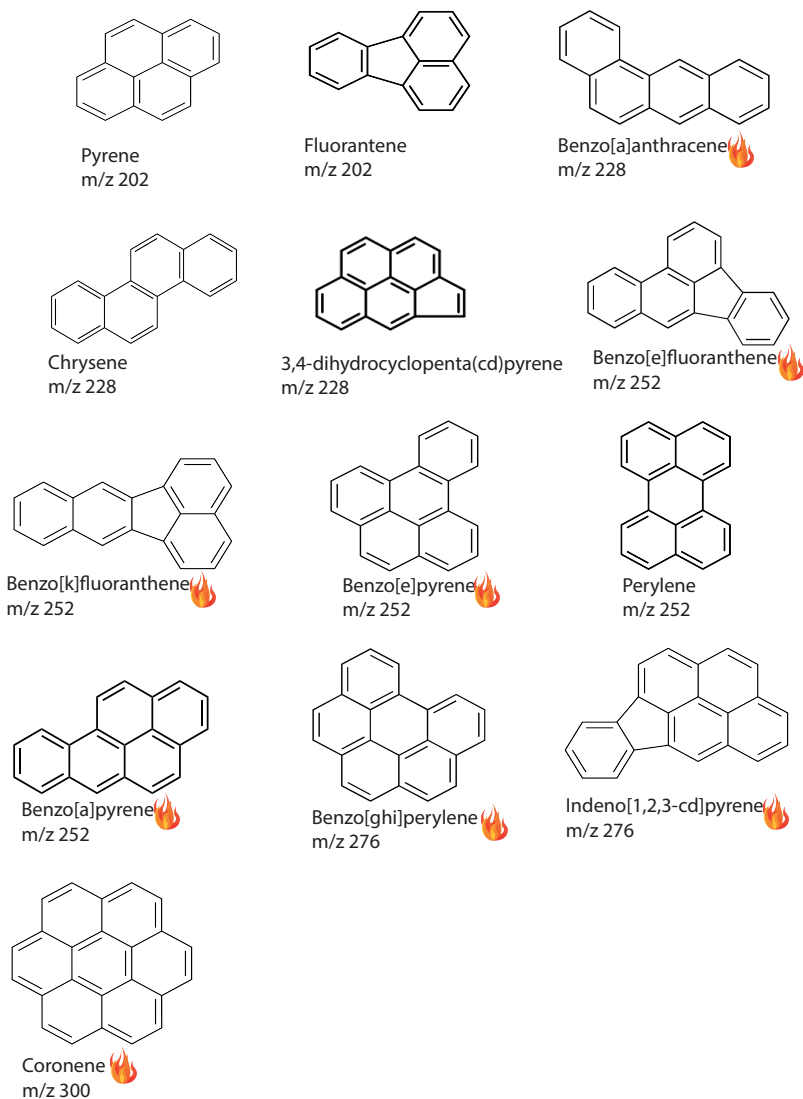
Plate 1. Structure, name and mass of high molecular weight PAHs. The fire-symbol indicates which PAHs are known to be combustion-derived.

PAHs have been studied in the Schandelah-1 core around the extinction interval, from the latest Triassic into the earliest Hettangian (Grüters, 2012). It was discussed that different sources explain the PAH concentrations in the Schandelah-1 core. As the PAH increase started around the same time as flood-basalt volcanism started, this volcanism is seen as a source. Due to the subsequent increase in greenhouse gasses, climate warmed, making wild fires more likely, being another source for the PAHs observed. The concentration of coronene has a significantly different pattern than other PAHs, which Grüters (2012) related to the Rochechouart impact (201 ±1 Ma, figure 6). However, the specific carbon isotopes of the PAHs indicate a terrestrial origin of the PAHs. Thus, PAHs found in the Schandelah core around the TJB can be directly and indirectly linked to CAMP volcanism (Grüters, 2012).

2.4   Ecological turnover

In the marine realm, invertebrates like bivalves and ammonoids were heavily affected by the ETE, but the extinction was most catastrophic for reef communities. Recovery of reef carbonate production was slow and lasted over 10 million years, while many other ecosystems recovered within 2 million years (Flügel & Kiessling, 2002), comparable to the recovery rate (genera/million year) after the end-Permian extinction (Schaltegger, *et al.*, 2008). The terrestrial plant record seems somewhat less affected by the end-Triassic extinction, though most sections do indicate a significant extinction event with a great loss of Triassic species and a disappearance of approximately 40% of terrestrial tetrapod families (Olsen *et al.*, 1987; Fowell & Olsen, 1993; Hallam & Wignall, 1997). Palynology is a widely applied method for investigating ecosystem variations. However there can be differences in the losses and vegetational turnover observed in palynology and macrofossils (Bond & Grasby, 2017). In most sections studied for palynology, the boundary interval is unique with a high fern spike, such as Northern and Southern Germany, the Newark Basin (USA), and St. Audries Bay (UK) (van de Schootbrugge, *et al.*, 2009; Deenen *et al.*, 2010). Globally, the terrestrial record indicates a large turnover and disturbance in plants (Bond & Grasby, 2017).

Reproductive processes of terrestrial plants also show increased stress around the extinction interval, with increased amounts of mutagenic aberrant spores in the Danish and North German basins. Also in the Schandelah-1 core increased levels of aberrant spores have been found close to the TJB (Bos, unpublished data). Abnormal spores and pollen have also been found across the Permian-Triassic boundary, which is suggested to be caused by volcanic pollution of the Siberian Traps (Visscher *et al.*, 2004; Hochuli, *et al.*, 2017).

Abbink (1998) and Abbink *et al.* (2004) proposed a Sporomorph Ecogroup (SEG) model for Northwest European Jurassic paleocommunities, based on the assumption that climate and geography are largely controlled by stress and disturbance. Thus, variations in SEG abundances reflect changes in climate or geography. This enables us to make interpretations of the distribution of Jurassic sporomorphs in terms of paleoenvironmental changes, in Northwest Europe. Before sporomorphs can be divided into ecogroups, it is important to note the difference between stress and disturbance. As defined by Grime (1977), stress is any condition that limits plant biomass production, while disturbance is any condition or process that causes destruction of plant biomass. The variation between high or low stress and high or low disturbance in plant habitat results in specific surviving strategies (Grime, 1977). These life strategies are used for SEG definitions by Abbink (1998). Communities with low levels of stress and disturbance are grouped under 'Lowland', due to the favourable conditions. Other SEGs are defined by additional stress or disturbance. In total 6 different ecogroups have been defined by Abbink (1998), namely upland, lowland, river, pioneer, coastal and tidal.

3 Materials and method

3.1 Position and lithology of the Schandelah-1 core

The Schandelah-1 core was obtained in 2008 near the village Schandelah in Lower Saxony, Germany (figure 7). The core reaches 338 mbs and the lithology spans the Rhaetian up to Toarchian. The entire core was logged and photographed, and then sampled at 10 cm intervals. Details of the core and the drilling are described in van de Schootbrugge *et al.*, (2018).
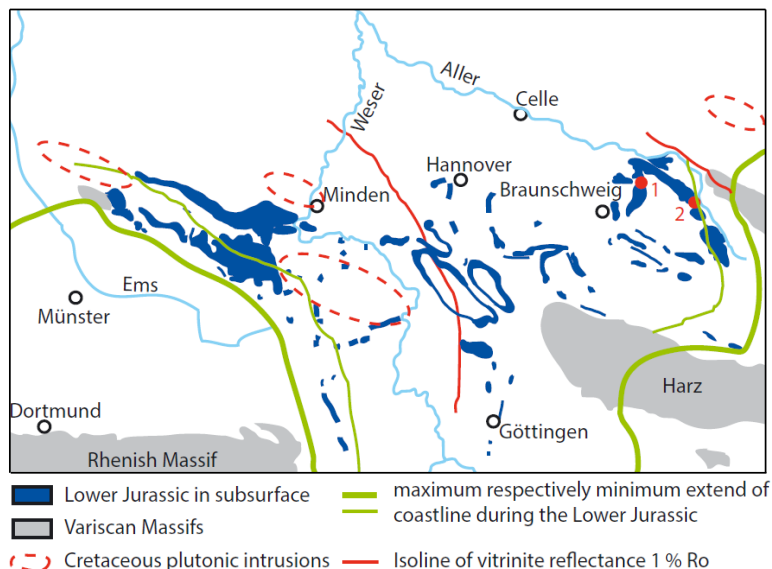
Figure 7: Location map of the drilling site, indicating the occurrences of Lower Jurassic sediments and Cretaceous intrusions. Location 1 is the Schandelah-1 core; 2 is the Mariental-1 core. Retrieved from van de Schootbrugge *et al.*, 2018.

The top of the Rhaetian belongs to the Exter formation, which contains the end-Triassic extinction event and has a large variation in sedimentological features (van de Schootbrugge *et al.*, 2018). Most of the Exter formation is characterized by medium-grained, current-rippled sandstone with thin mud divisions, including abundant plant material and charcoal. The Exter formation is subdivided in two beds, starting at the Contorta beds, followed by the thick Triletes beds consisting of fine-grained sand- and siltstone. The Triletes beds are capped by a sharp surface which is the transition to the different facies of the Psilonoten sandstone at the TJB. The Hettangian is found at depth from 318.6 to 233.3 mbs, and correspond to the Angulatenon formation (figure 9). The lower Hettangian consists of laminated mudstones with intervals containing paper shales. The rest of the Hettangian in the Schandelah-1 core consists mainly of silt- and sandstone lenses with cross-bedding, bioturbation and/or reworking, interbedded with organic rich mudstones and shales. The depositional environment was a semi-restricted shallow marine, containing deltaic to shelf sediments. Two intervals stand out in the Hettangian, within the upper half of the Angulata ammonite zone. These intervals are distinctly red-coloured laminated claystones at 254.8 - 258.65 mbs and 234 - 238 mbs (van de Schootbrugge *et al.*, 2018). This study is focused on the Upper Hettangian around these red claystones, at the interval from 270 to 230 mbs.
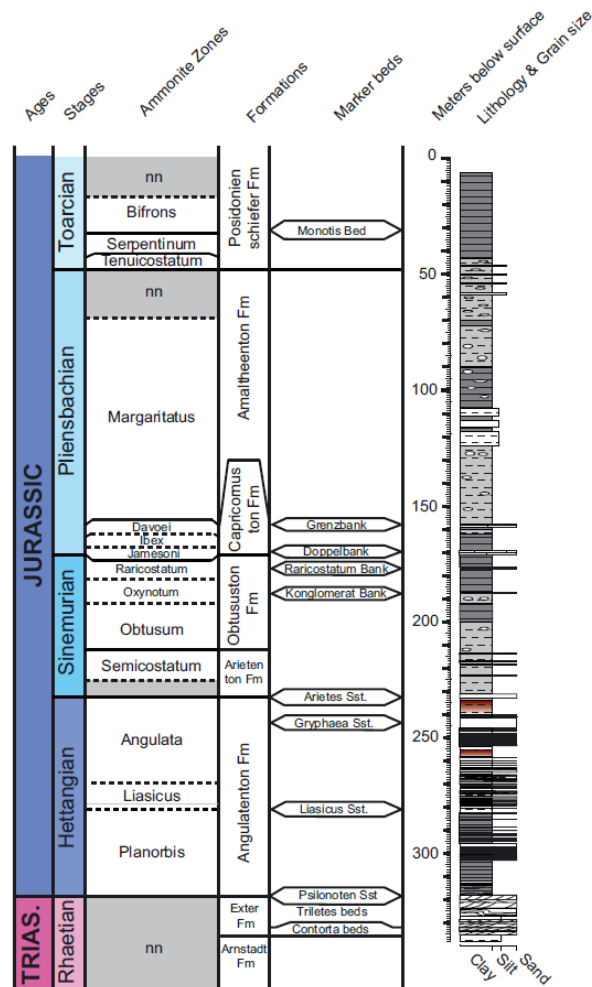
Figure 8: Ages, stages, ammonite zones, formations, marker beds, depth and lithology in the Upper Triassic and Lower Jurassic in the Schandelah-1 core. 'nn' means no ammonite zone defined due to a lack of ammonites. Retrieved from van de Schootbrugge *et al.*, 2018.

3.2   Age model and biostratigraphy

Ruhl *et al.* (2010) established an astronomical timescale for the Hettangian sediments at St. Audrie's Bay, SW England, located in a more westward basin within the European Epicontinental Sea. This time-scale is based on meters-thick cycles in limestone and shale, as well as variability in chemical and physical proxy records. 3 to 5 variations were found within these meter-scale cycles, which are interpreted as precession-controlled climatic variations within the 100 kyr eccentricity cycle. 18 of these 100 kyr eccentricity cycles have been found in the Hettangian, indicating a duration of 1.8 Ma if this eccentricity cycle is stable in duration. Huang (2018) uses a tuning with the stable 405 kyr cycle, which gives an astronomically constrained duration of the Hettangian of 1.97 Ma, which is in line with the Geological timescale 2012 (Gradstein *et al.*, 2012).

Van der Weijst (2015) has applied spectral analysis on multiple Hettangian to Early Sinemurian records from the Schandelah-1 core. This study indicates in-phase regular alternations in magnetic susceptibility, δ $^{13}C_{org}$ and S/P ratio, with an average thickness of 21.4 to 26.7 m. Van der Weijst (2015) suggests that this could represent the 405 kyr eccentricity cycle, with a potential astronomical

tuning that fits previous assessments of the Hettangian. Although uncertainties over the timing and interpretation of the regular alternations are acknowledged, it is clear that astronomical cyclicity did affect the climate of the European Epicontinental Sea in the Hettangian to a certain extent.

Within the Rhaetian of the Schandelah-1 core, no ammonites, foraminifers or ostracods are found, making ammonoid biozonation, which is commonly used, impossible (van de Schootbrugge *et al.*, 2018). After the Rhaetian, ammonites remain in low abundance. Dinoflagellates, pollen and spores however are useful and reliable biostratigraphic tools for placing stage boundaries. In the latest Triassic, several pollen species like *Ricciisporites tuberculatus*, *Ovalipollis ovalis* and *Lunatisporites rhaeticus* stop occurring at 319.50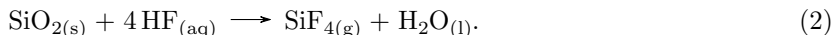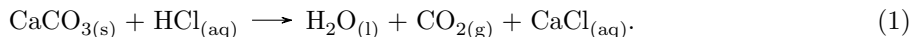 mbs, making this the deepest level for the Triassic-Jurassic boundary (van de Schootbrugge *et al.*, 2018). The common occurrence of typical Early Jurassic species mark an abrupt change in palynofacies at 318.2 mbs. The TJB is thus located between 319.5 and 318.2 mbs. A sharp organic carbon isotope excursion, the Spelae CIE, is correlated to the isotope record of the nearby Mariental-1 core and places the TJ boundary at 318.6 mbs, at the base of the Psilonoten sandstone (van de Schootbrugge, *et al.*, 2018). The ammonite *Psiloceras spelae*, the marker species for the base of the Jurassic at Kuhjoch (GSSP) (von Hillebrandt *et al.*, 2007), first occurs at 312.20 mbs within the Lower Hettangian. In the Hettangian all ammonite zones could be assigned, although boundaries are inconclusive due to low abundances. The Hettangian-Sinemurian boundary is placed at 233.3 mbs based on the last common occurrence of dinoflagellate *Dapcodinium priscum* and the first occurrence of nannofossil *Parhabdolithus liasicus* (van de Schootbrugge, *et al.*, 2018).

3.3 Palynology

A total of 30 samples were prepared for palynological assessment. Of these, 14 old residues could be re-used for new slides, and 16 new samples have been prepared. For preparation, approximately 3 grams of crushed samples were spiked with a known amount of Lycopodium spores (batch no. 140119321; 19855 spores per tablet), in order to quantify the absolute number of palynomorphs per gram. The old residues were spiked with 20848 Lycopodium spores per sample. A standard palynology treatment was applied using a combination of 10% hydrochloric acid (HCl) and 38-40% hydrofluoric acid (HF) to dissolve carbonates and silicates respectively:

$$CaCO_{3(s)} + HCl_{(aq)} \longrightarrow H_2O_{(l)} + CO_{2(g)} + CaCl_{(aq)}. \tag{1}$$

$$SiO_{2(s)} + 4\,HF_{(aq)} \longrightarrow SiF_{4(g)} + H_2O_{(l)}. \tag{2}$$

The remaining residue was sieved using a 10 μm fraction nylon mesh sieve to collect palynomorphs. The subsequent residual material was homogenized and permanently mounted on a slide for light microscopy analysis.

Slide material was analyzed with 630x and 1000x magnification, until a minimum of 300 palynomorphs were identified. Sporomorph taxonomy follows from e.g. Mehlqvist, *et al.*, 2009; Heunish *et al.*, 2010; Lindström, 2016 and van der Schootbrugge *et al.*, 2018. Aberrant spore occurrences were identified and classified based on the classification scheme of Lindström *et al.*, 2019 (figure 9). In order to extract ecological and geographical parameters from the palynology assemblages, all palynomorphs were divided in ecological classes based on the sporomorph ecogroup model (Abbink, 1998; Abbink, 2004; van der Weijst, 2015).

3.4 Organic extractions of PAHs

For PAH extractions, 12 samples were selected throughout the section of 230 to 260 m depth in the Schandelah-1 core; 6 within and 6 around the red intervals. Approximately 15 - 17 grams of powdered sample (<0.2 mm) was extracted using the Milestone Microwave Extractor Ethos-X, with a mixture of dichloromethane (DCM) and methanol (MeOH) (9:1) as solvent. The program duration was 60 minutes, starting with a 20 minute heating from 20°C towards 70°C, then keeping the temperature
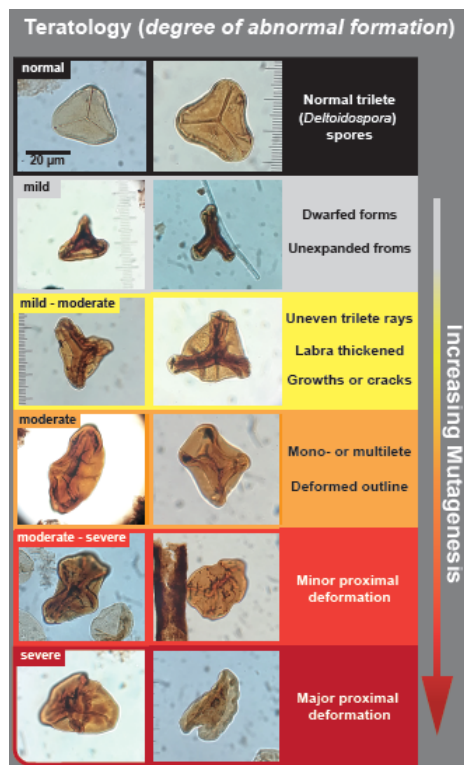
Figure 9: The classification of aberrant smooth, triangular, trilete spores, arranged after teratology category as defined by Lindström *et al.*, 2019. Retrieved from Bos *et al.*, 2020

constant at 70°C for 10 minutes, followed by a cooling down of the system back to 20°C over 30 minutes. The extracts were separated from sediments and other solids using a sodium sulphate column using DCM to rinse. For sulphur removal, activated copper granules and DCM were added to the extracts and was stirred for 24 hours. The total lipid extracts were separated in three fractions using silica gel column chromatography (4 cm), based on the procedures of Nabbefelt *et al.*, 2010 and Song *et al.*, 2020. Firstly, the saturated fraction was separated with Hexane, using 2 times the volume of the silica gel column. The aromatic fraction was separated using a Hexane/DCM (1:1) solution, using 2 to 3 times the volume of the silica gel column. The remaining polar fraction was obtained by an excess of DCM/MeOH (1:1) solution. Toluene (approximately 300 μL per 1 mg) was added to the dried aromatic fraction.

The aromatic fraction was measured by gas chromatography (GC), which separates compounds in gas phase. Helium was used as carrier gas and the different compounds came out of the capillary column at specific retention times, based on the amount of carbon in the compounds. GC results were used as a check for toluene concentrations, as the right concentration was needed for the right signal strength. If the signal was too strong or too weak, the concentration of toluene could be adapted. Afterwards, 1 μL of the aromatic fractions were run in the gas chromatogram mass spectrometer (GC-MS) to obtain information on the masses of the molecules in the chromatogram and identify peaks representing PAHs. 2 different GC-MS were used, the Trace GC Ultra coupled with the Trace DSQ (Thermo-Fisher Scientific) and the Agilent Technologies 7890B GC system coupled with the Agilent 5977B MSD. The DSQ was used after technical malfunctions of the Agilent GC-MS system. Both the GC and GC-MS systems were run for 70 minutes. Separation was achieved using a capillary column (25 m x 0.32 mm x 0.12 μm) in both systems. 4 to 7-ringed PAHs (mass $\geq$228) were identified in all samples. A combination of 1 μL of the aromatic fractions along with 1 μL of 1.1-binaphthyl standard

(0.1 mg/ml) were co-injected in the GC-MS for quantitative analysis, using the SIM-method. This method allows us to single out m/z 228, m/z 252, m/z 276 and m/z 300 ions belonging to PAH compounds with 4 to 7 rings, in addition to identifying the main peak of the 1.1-Binaphthyl standard (m/z of 252).

3.5   PAH quantification

The GC-MS chromatograms were integrated using the XCalibur software (ThermoFisher Scientific), to obtain surface areas for every peak representing a PAH. These surface areas were compared to the area of the standard according to formula (3):

$$\text{PAH}_{\text{uncorrected}} \ (\mu\text{g}) = \frac{\text{amount}_{\text{1.1-Binaphthyl standard}} * \text{area}_{PAH}}{\text{area}_{\text{1.1-Binaphthyl standard}}} \tag{3}$$

These uncorrected PAH concentrations need to be corrected for the volume of added Toluene, the amount of sediment extracted per sample and the difference in peak surface between the GC and GC-MS (4). This was done by comparing the surfaces of the 1.1-Binaphthyl standard with a Coronene standard in both the GC and both GC-MS types (5), so that each sample could be corrected for the right GC-MS.

$$\text{PAH}_{\text{corrected}} = \frac{\text{PAH}_{\text{uncorrected}} \ (\mu\text{g}) * \text{total volume Toluene} * \text{correction value}}{\text{amount of sediment (g)}}. \tag{4}$$

$$\text{Correction value} = \frac{\text{Coronene}_{GC-MS}/\text{1.1-Binaphthyl}_{GC-MS}}{\text{Coronene}_{GC}/\text{1.1-Binaphthyl}_{GC}} \tag{5}$$

This amount of PAH was corrected for the amount the was already lost by earlier measurements. As some samples had already been measured multiple times, this loss of sample was important to take into account.

Finally, the amount of PAH was corrected for the total amount of organic carbon in the sample (6). This gives the PAH values in μg / g TOC.

$$PAH(\mu g/gTOC) = \frac{\text{Amount of PAH}_{\text{corrected}}}{(\text{TOC (\%) * amount of sediment (g) })/100}. \tag{6}$$

As this method has never been used in this lab before, the precision in the PAH data is unknown. Four samples (255.6, 251.2, 236.1 and 232.1 mbs) have been measured in duplicate, in order to obtain some constraint on the precision of the method. From these, 251.2 was easiest to integrate, while the other 3 had a less constant baseline, making the integrated surfaces more subjective.

The specific PAHs have been identified based on their retention time, in comparison to the work of Naraoka $et\ al.$, 2000; Nabbefeld $et\ al.$, 2010 and Grüters, 2012.

4 Results

4.1 Spore and pollen distribution

The close proximity of the Schandelah-1 core to the paleo-shoreline resulted in the dominant abundance of terrestrial palynomorphs (spore and pollen) in the Upper Hettangian. Most common sporomorphs are shown in plate 2 (appendix), and the total counts are presented in table 2 (appendix). The relative abundance of a selection of common palynomorphs and marker species are shown in figure 10. The palynological assemblage is dominated by *Perinopollenites elatoides*, which has a relative abundance of 25 to 45% in most of the Upper Hettangian, but decreases to only 10 to 20% inside the red intervals, with the largest decrease in the lowest interval. *Concavisporites* spp. and *Deltoidospora* spp. are the most common spores, where the later is more common throughout the entire section. Both spore abundances increase around 100% in the lower red interval, and have a smaller increase in the upper red interval. Bisaccate pollen, originating from coniferous trees, have no distinct change throughout the section, while the pollen *Classopollis*, whose source is another coniferous family, does have lower abundances in the red intervals. *Cerebropollenites* is considered a marker species for the Sinemurian (Larsson, 2009) but occurs throughout the studied Upper Hettangian section. The highest abundance does occur in the lowest Sinemurian with a relative abundance over 4%, but this is not a large increase compared to the Hettangian. *Dapcodinium priscum* is considered a marker species of the Sinemurian, with the LO placed at the Hettangian-Sinemurian boundary. However, it was observed at a depth of 232 mbs, within the lowest Sinemurian.
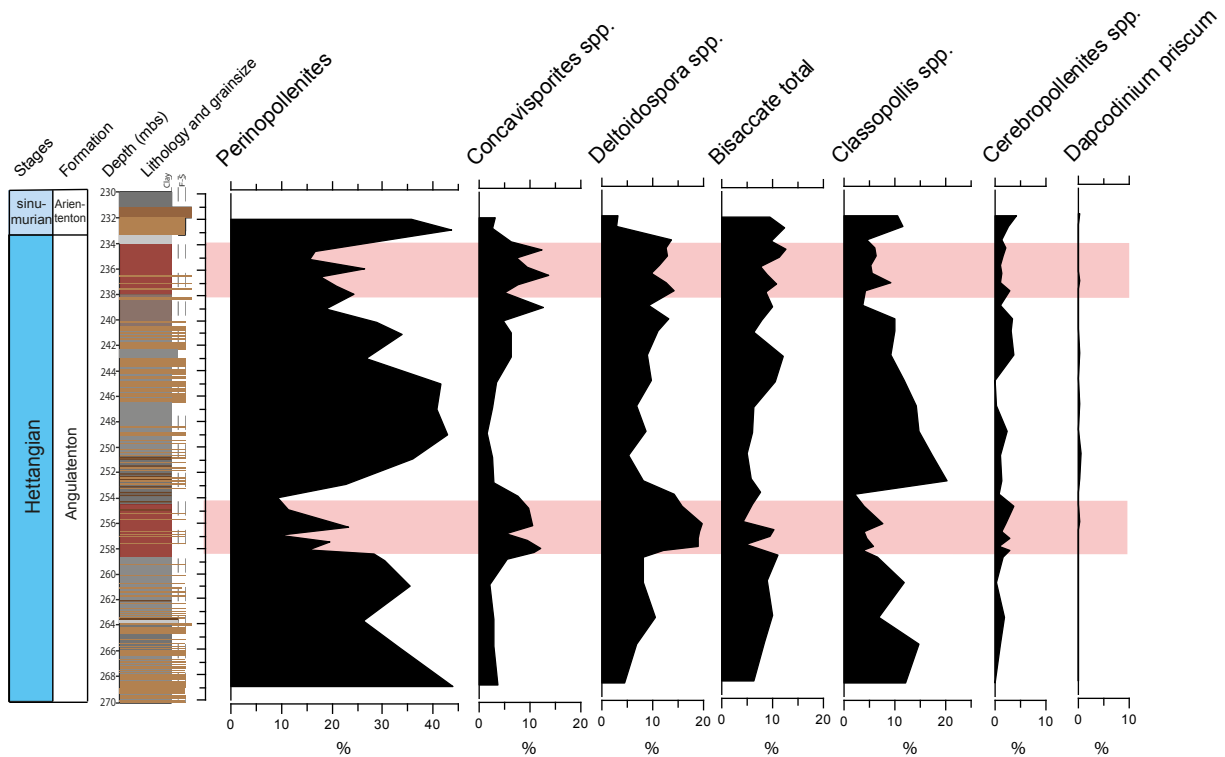
Figure 10: Relative abundances of a selection of common palynomorphs and marker species.

Based on the spore/pollen ratio (S/P), two clear fern spikes can be identified which coincide with the red-clay intervals of the Upper Hettangian (figure 11). Within these fern spikes, mainly *Concavisporites*

spp., *Deltoidospora* spp., *Trachysporites fuscus* and *Acanthotriletes varius* are abundant. Within the fern spikes approximately 50% of the sporomorphs are spores (S/P ratio around 1), compared to only around 30% (S/P ratio around 0.3) in the rest of the studied section. In addition, elevated aberrant spore abundances, clearly above background conditions of 5%, correspond to the same intervals (figure 11). However, a similar increased spore aberration is observed for the interval directly between the red clays, around 248 - 242 mbs (indicated with a dashed rectangle in figure 11). In this interval the spore/pollen ratio is low, with only around 30% of all sporomorphs being spores, which may result in unreliable aberrant spore estimates. Most aberrant spores have mild, or mild-to-moderate teratology, often being dwarfed and unexpanded forms, with aberrant folding, uneven trilete rays or with thickened labras (plate 3, appendix; after Lindström *et al.*, 2019). Severity seems to increase with higher abundances of aberrations. However, this trend is not consistent with occasional high severity in low aberrant samples, and low severity in high aberrant samples. Reworking of mostly Triassic palynomorphs, such as *Aulisporites* sp. and *Ricciisporites tuberculatus*, is significantly higher within the red intervals than the rest of the section. Mainly the lowest red-clay interval has high amounts of reworking, up to 10% of all palynomorphs. This is less in the upper red interval, having only up to 5% reworking. Outside these red intervals, reworking generally does not exceed 2%. The absolute number of palynomorphs per gram sediment shows large variations within the studied section (figure 11). Abundances are clearly lowest around the two red-clay intervals, also having a rather low variability of 5000 up to 25000 palynomorphs per gram sediment. Outside the intervals abundances can have a much higher variation between 5000 and 140000 palynomorphs per gram.
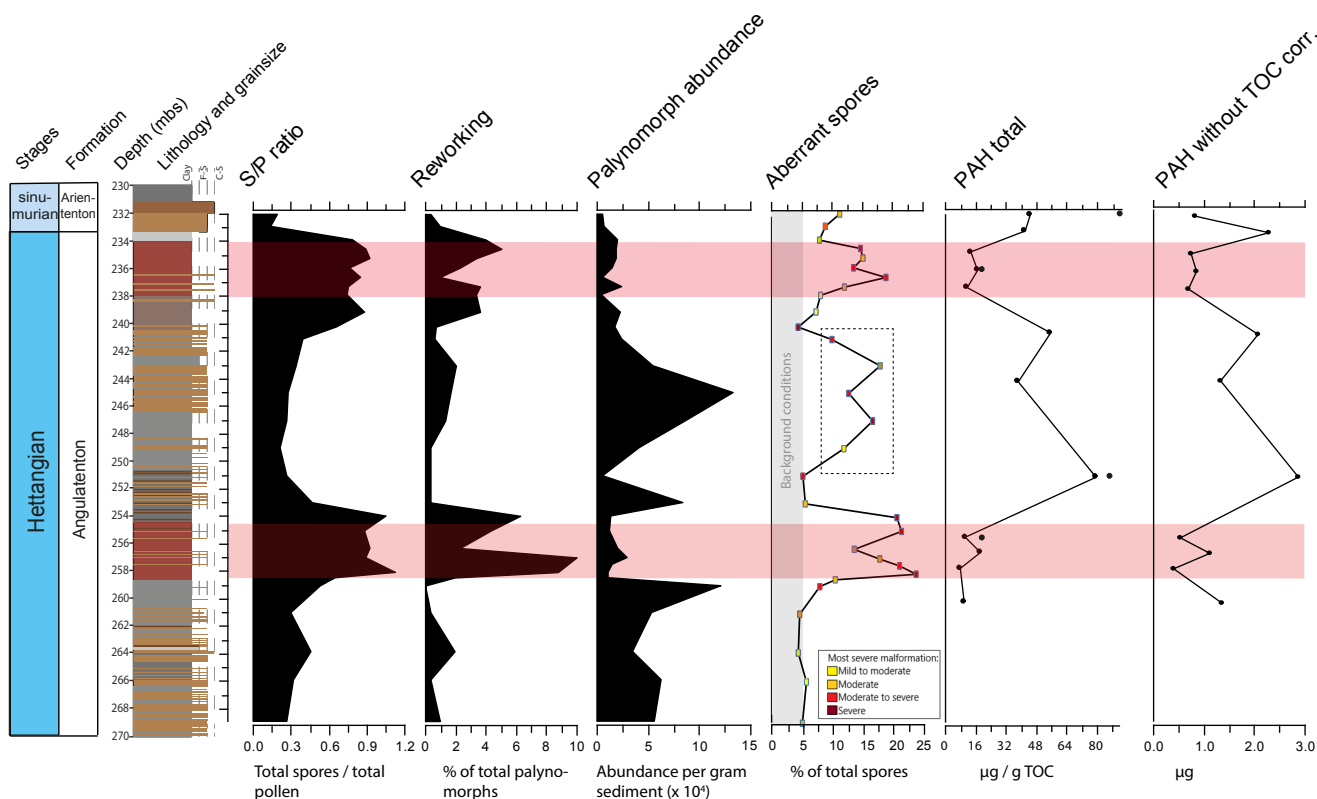
Figure 11: From left to right: spore to pollen ratio, amount of reworking, abundance of palynomorphs per gram sediment, amount and severity of aberrant spores, the total PAH concentrations, including the duplicate measurements, and the total PAH concentrations without TOC correction. The red intervals are highlighted by red bars.

Palynomorphs of the Upper Hettangian are grouped according to previously defined sporomorph ecogroups (table 3 (appendix); Abbink, 2004; van der Weijst, 2015). This enables us to assess the distribution and dynamics between the ecological groups (figure 12). The group representing a tidal ecosystem did not exceed 1% and is absent for most of the Upper Hettangian. Therefore, this group is not incorporated into the overall assessment. Some sporomorphs are not attributed to an ecological group and are grouped under N/A, along with all undetermined spores and pollen. From figure 12 it is clear that lowland is the most abundant ecological group, with 25 to 50% of palynomorphs originating from the wet lowland. A decrease in wet lowland abundance occurs around the first red interval, coinciding with an increase in dry lowland and river groups. A similar decrease in wet lowland and increase in dry lowland and river occurs in the upper red interval, but with a lower intensity. The other ecological groups do not vary that distinctly between the red intervals and the rest of the section. Marine palynomorphs are very limited in abundance throughout the section.

Not every palynomorph could be identified. Some slides contain high amounts of debris, which can cover palynomorphs making them unidentifiable. There is no clear trend in the amount of unknowns. Besides palynomorphs, other particles have been identified, for example zircons, charcoal, insect remains and butterfly scales. Of these, only the amount of zircons was traced throughout the samples (table 2, appendix).
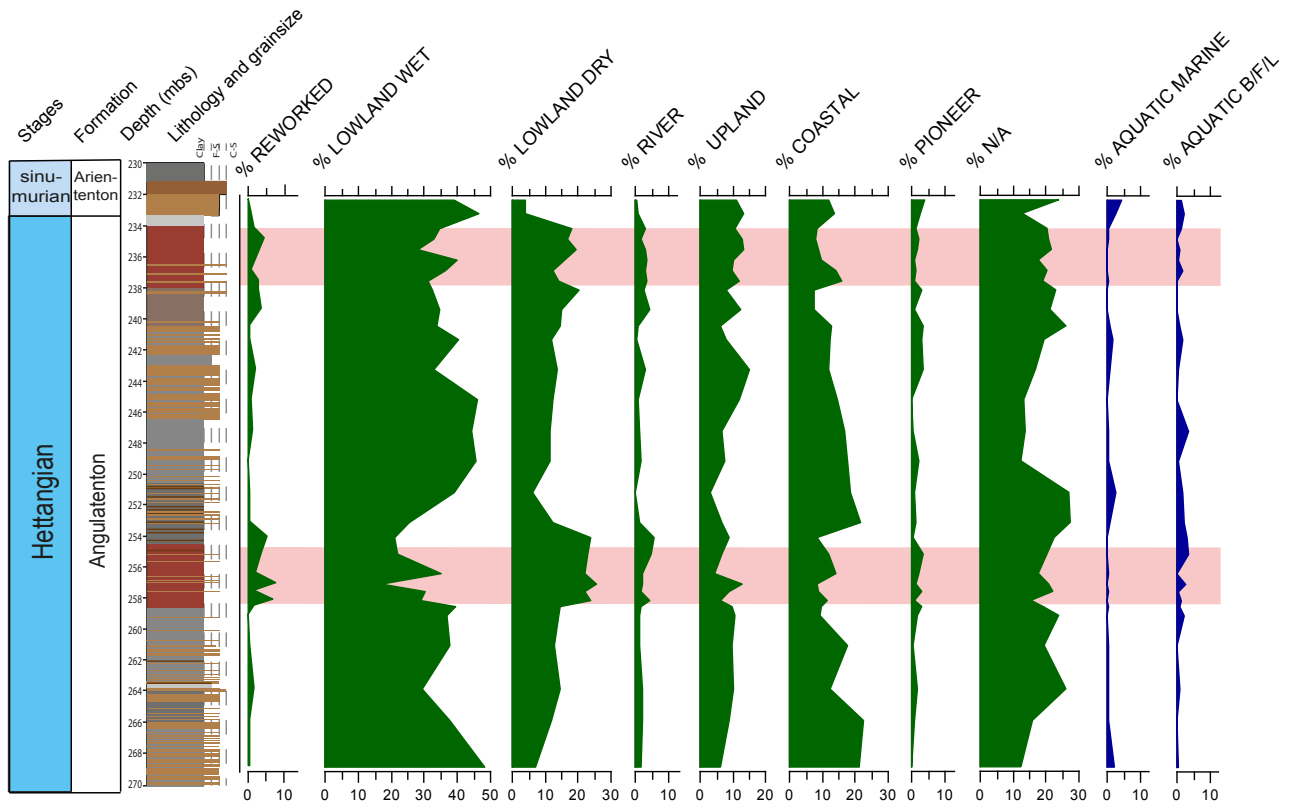
Figure 12: Distribution of ecosystems using the sporomorphs ecogroup model based on Abbink (2004) and van der Weijst (2015), and the amount of reworking. Green colours are based on terrestrial palynomorphs, blue by aquatic palynomorphs. N/A: not attributable. B/F/L: brackish, freshwater and lagoonal.

4.2 PAH distribution

The chromatograms of PAH extractions of the aromatic fractions with the standard setting (scanning for m/z 50 - 800) indicate the presence of multiple PAHs, but other compounds are also present in the samples. Figure 13 shows a chromatogram on top, and a selection of specific masses m/z 300, 276, 252 and 228 underneath. The PAHs are located in the chromatogram at the peak of the specific masses, indicated with the dashed line. While the PAHs can be located in the chromatogram, integration of such a chromatogram is subjective due to the other compounds interfering within the wide peaks of the PAHs. Therefore only the results using the SIM mode, scanning only for the m/z 228, 252, 276 and 300, are used for quantification, as they contain more precise information on the PAHs by not measuring other compounds.
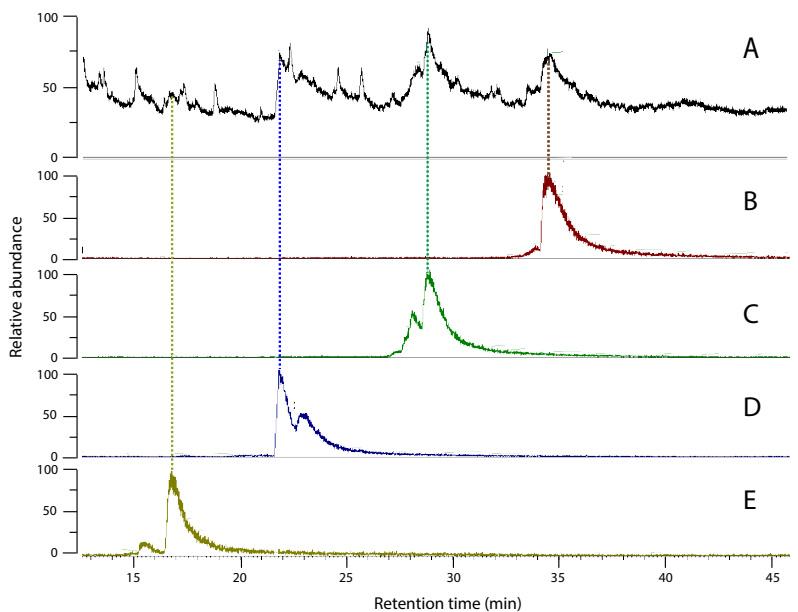
Figure 13: (A) A total ion chromatogram using the standard GC-MS setting, scanning for m/z of 50 to 800. Underneath: a selection of the retention times where only (B) m/z 300 is measured, (C) m/z 276 is measured, (D) m/z 252 is measured and (E) m/z 228 is measured. The dashed lines visualise which mass is responsible for which peak in the chromatogram.

PAH isomers have been quantified individually, and these results added up gives the total concentration of all heavy PAHs present in a sample (table 1, appendix). This sum of all heavy PAHs together have been plotted as PAH total in figure 11. In the red intervals, the total PAH concentrations are lowest, staying under 18 μg/g TOC, while concentrations are higher between the red layers, reaching up to 90 μg/g TOC.

PAH is corrected for TOC content because PAHs are part of the total organic carbon, and less organic carbon in the sediment can be an indication that either less is produced or less is preserved. This correction results in higher PAH concentrations when TOC is low, and lower PAH concentrations when TOC is high. However, without this correction for TOC, a similar trend is observed in PAH content, meaning that the TOC concentrations do not highly influence the PAH results (figure 11).

Individual PAH isomers could be recognized quite well. Chrysene and Triphenylene are not always fully separated in the GC-MS, therefore it is uncertain whether that peak represents Chrysene, Triphenylene, or a combination of both. All other PAH are specific to one peak in the chromatogram. The

concentration of all identified PAHs through the Upper Hettangian is shown in figure 15 (note different scales on the x-axis). Almost all PAHs show a lower concentration within the red intervals than the part in between; some are even absent in the red clay intervals. Only Benzo(a)anthracene has slightly higher concentrations within the red intervals, but its concentration remains low, under 2 μg/g TOC. Most PAHs have their highest values between the red intervals at 251.2 mbs or at 240.7 mbs.

PAH concentrations in figure 15 mostly follows the trend of the total PAH in figure 11. Comparing the distribution of the PAH isomers to the total PAH can give insights on the relative abundance of the different PAHs. The relative abundance of the four different masses are plotted in figure 14, including the four duplicate measurements. It can be observed that for m/z 228 and m/z 252, the relative abundances are quite average during the red clay intervals. M/z 276 has a distinct lower abundance during the red intervals, while m/z 300 (Coronene) has a higher relative abundance in these depths. Thus, although the total concentration of PAHs is low within the red clay intervals, the distribution between the different masses indicates a larger contribution of coronene within the red intervals.
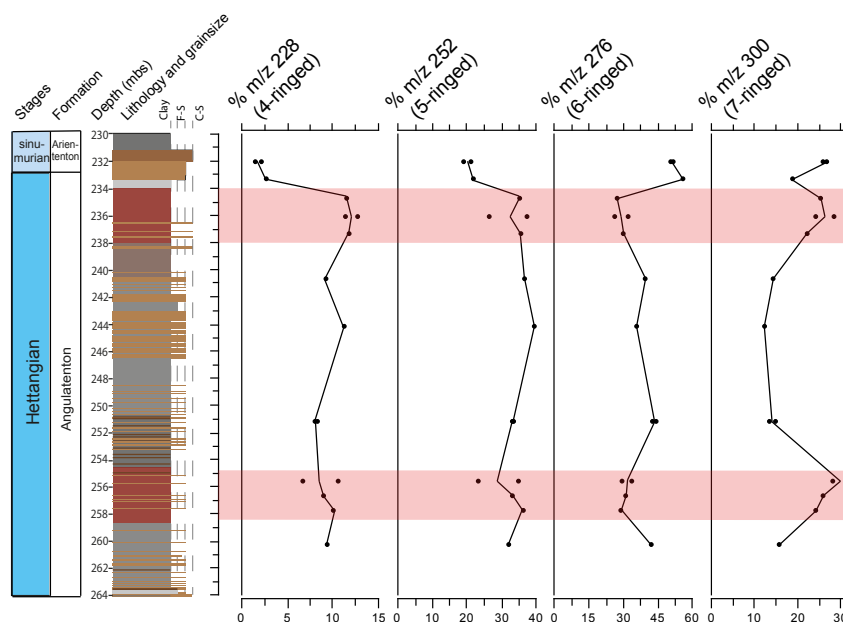
Figure 14: The relative abundance of the different masses of polycyclic aromatic hydrocarbons. The red intervals are indicated and results from the duplicate measurements are included.
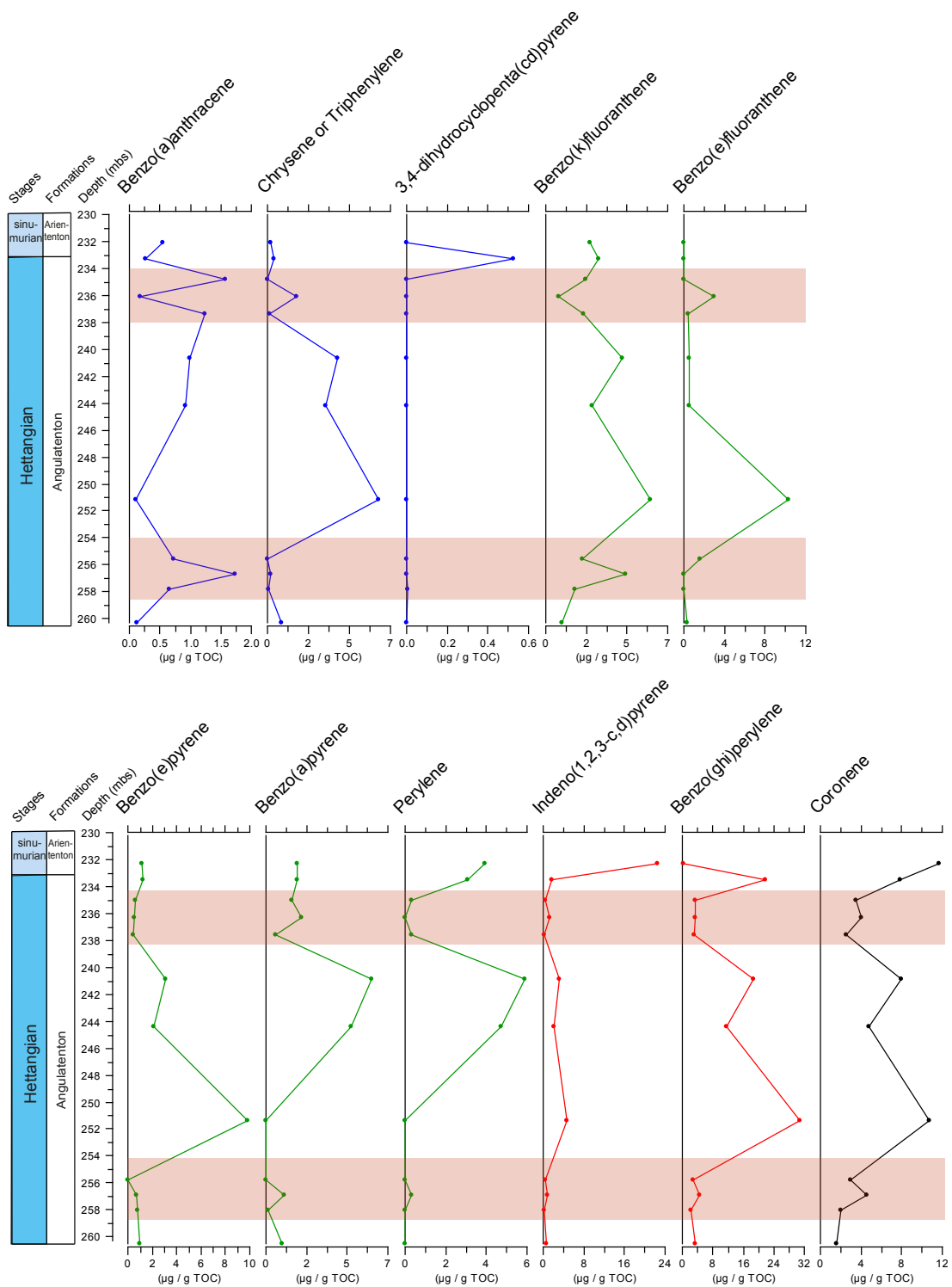
Figure 15: Concentrations of specific PAHs throughout the studied section. The red intervals are highlighted. The colour of the graphs indicate the molecular weight of the PAH (Blue = m/z 228; green = m/z 252; red = m/z 276 and black = m/z 300. The scale on the x-axis varies per PAH.

5 Discussion

5.1 Lithology and depositional environment

Seismites have been observed in multiple locations in Europe close to the extinction interval, including in the Schandelah-1 core (Lindström *et al.*, 2015; van de Schootbrugge *et al.*, 2018). These earthquake induced soft-sediment deformations could be explained by strong earthquakes caused by either the onset of intense CAMP eruptions or a meteorite impact (Lindstrom, *et al.*, 2015; Wignall & Bond, 2008; Bond & Grasby, 2017). As no fully supporting evidence is found for a large enough meteorite impact with this timing, and due to the repetitive character of the seismites, CAMP eruptions are the most plausible explanation (Lindström *et al.*, 2015). This widespread seismicity co-occurred with terrestrial disturbances in ecosystems in the Late Triassic, prior to the main carbon isotope excursion (figure 16). There is no evidence of such soft sediment deformation in the Hettangian (Lindström *et al.*, 2015; van de Schootbrugge *et al.*, 2018), which indicates that if volcanism played a role in the Upper Hettangian, eruptions were not similar to the start of CAMP volcanism and did not cause heavy earthquakes in this area.

The lithology in the red intervals does not differ much from the rest of the Upper Hettangian, being mainly clays with sandstone lenses. Only the colour in these two intervals is distinctly different. This similar lithology indicates that the depositional environment was not distinctly different at the times of red clay deposition, and there is no indication for a distinct change in silisiclastic input. XRF measurements have indicated relative high iron concentrations in the red intervals (figure 16). The red colour of the claystones and relatively high iron concentrations in these beds suggest increased oxidation.

5.2 Preservation

Where the total organic carbon (TOC) in the sediment is low, there is also a low abundance in palynomorphs (figure 16). This is mainly within the red intervals, and seems to indicate either a low preservation due to oxic degradation, or low productivity of organic matter in these intervals. Increased oxidation in the red intervals could explain the low preservation of organic matter in these intervals, as only organic matter that escapes oxidation in marine environments gets preserved (Canfield, 1993). Thus the red intervals could have a lower preservation of palynomorphs than the rest of the Upper Hettangian. When less organic matter is preserved, it is likely that less resistant, marine organic material is lost earlier. This could present a bias in the preserved record, which might also explain the positive carbon isotopes within the red intervals (figure 16). Bartolini *et al.*, (2012) presented increases in carbon isotopes at marine localities in modern England, Greenland and America, in waters in or connected to the EES (figure 4). It is possible that the whole EES experienced two periods of increased oxic conditions, due to increased mixing of seawater or changes in precipitation. This increase in oxidation matches with the positive excursions in the carbon isotopes.

Biodegradation has been studied as a new proxy on the Schandelah-1 core, using the smooth trilete spores *Deltoidospora sp.* and *Concavisporites sp.* (Hollaar, 2017). High degrees of biodegradation are assumed to represent healthy and balanced ecosystems, with developed soils with microbial activity. Two drops in biodegradation occur within the red clay intervals. Hollaar (2017) explained this decrease in biodegradation as an ecosystem perturbation with degraded soils having a higher erosional flux of sporomorphs towards the marine system, leaving less options for microbial attack. This increased weathering is in line to the high degrees of reworking and soil loss described by van de Schootbrugge *et al.*, (in review). A decrease in biodegredation can result in well preserved palynomorphs, while above it was discussed that preservation was low. Finely preserved particles such as butterfly scales have been observed in the Upper Hettangian, also within the red intervals. Despite the low preservation of organic matter it might have been preserved due to the decrease in biodegradation.

Magnetic susceptibility has been studied by van der Weijst (2015) from the Late Rhaetian up to the Early Sinemurian (figure 17). Values reach up to 0.004 instrumental units in the lower red clay

interval, and up to 0.003 instrumental units the upper red claystone, clearly above the average of 0.001 throughout the Hettangian. Higher values in magnetic susceptibility can be linked to increased siliciclastic input by increased weathering or runoff (Ruhl *et al.*, 2010). These results are in line with the increase in weathering and erosion as described above.

Thus, high amounts of reworking, high magnetic susceptibility values and low amounts of biodegradation all point to increased weathering and erosion. The combination of less biodegradation (better identifiable) and a lower preservation (less identifiable) could be the cause that no trend was found in the amount of unknown palynomorphs, unknown pollen and unknown spores counted.

5.3   Vegetation dynamics

Palynological data is clearly different in the red intervals compared to the rest of the Upper Hettangian. The spore/pollen ratio, amount and severity of aberrant spores, and the amount of reworking are all higher within the red intervals, while the abundance of palynomorphs is clearly lower compared to the rest of the section. However, it is not tightly connected to the colour of the beds. As is shown in figure 11, these different values continue up a bit further than the lower red clay interval, which ends at 254.6 mbs while palynological data continues to be different up to at least 254.0 mbs. In the upper red claystone, the S/P ratio and reworking increases and the palynomorph abundance decreases slightly lower than the lithology changes colour, around 239 mbs compared to 238 mbs. It can be concluded that the red claystones do indicate more stressed environmental conditions during deposition, with other vegetational dynamics, a decrease in forests, and more reworking. However, this is not limited to the red colour as these conditions continue up higher than the lower red claystone, and started lower than the upper red claystone.

Increased amounts of aberrant spores have been found around the TJB in the Schandelah-1 core (Bos, unpublished data), as well in the Danish and North German basins (Lindström *et al.*, 2019). In the Schandelah-1 core aberrant percentages are low in the extinction interval but reach high concentrations right after the TJB. The same is observed in the data presented by Lindström *et al.* (2019), although they also found higher concentrations right before the TJB. Comparing the Upper Hettangian to the extinction interval shows that aberrant spore concentrations in the red intervals are high, and stay high for a relative long period, as is shown in figure 16. As the high degrees of aberrant spores around the TJB can be explained by increased disturbance on terrestrial ecosystems due to CAMP volcanism, similar degrees of disturbance can be expected as a cause for the Upper Hettangian aberrant spores. The aberrant concentrations between the two intervals are also quite high, but this might be caused by unreliable estimates as the total amount of spores are generally low. Whether these samples contain significant concentrations of aberrant spores, must be proven by analyzing more samples at a higher resolution. Also, identification of more than 300 palynomorphs might be useful to obtain high enough spore abundances for more representative aberrant percentages.

As presented in figure 12, sporomorph ecogroups indicate some changes in ecosystems at the red intervals. Lowland becomes dryer and there is an increase in river influence within the red intervals, being more apparent in the lower interval than the upper. This could indicate a shift in climate or precipitation patterns during the red clay deposition. Besides this observation, there are no large shifts of ecosystems in the Upper Hettangian, which limits the use in identifying the source of disturbance which caused the high amounts of aberrant spores in the red intervals.

Van der Weijst (2015) has also studied SEGs within the Hettangian in the Schandelah-1 core, but on a larger scale. There are differences between her Upper Hettangian results and those presented in this study. Although the largest SEG is also wet lowland in her study, a higher abundance is found within the lower red interval, in contradiction to this study. On the other hand the increases in the dry lowland and river SEG are more similar in the two data sets. This discrepancy raises the question how reliable this data is for conclusions on small scale vegetational patterns.
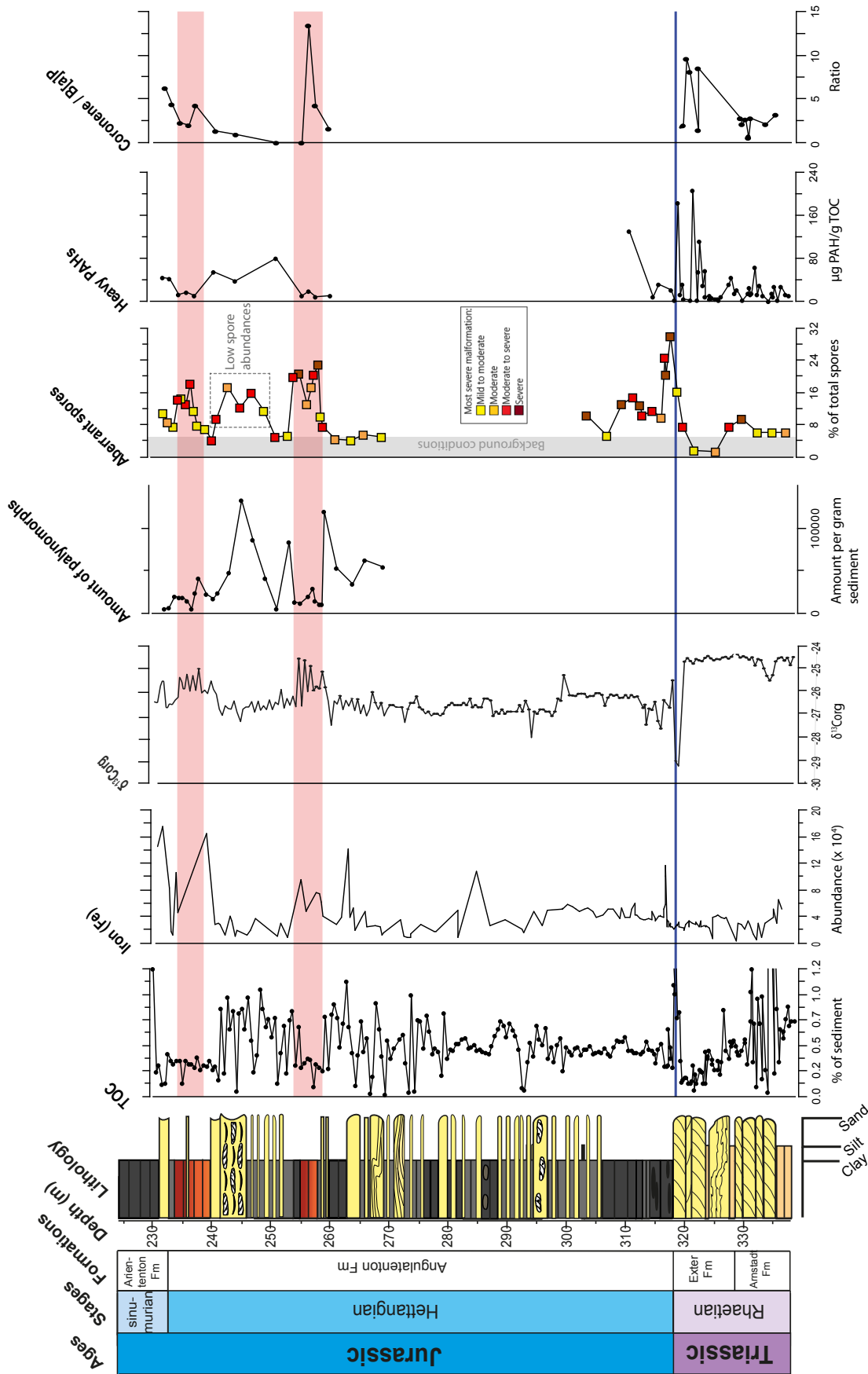
Figure 16: Data from left to right: The % of total organic carbon (TOC) in the sediment, excluding 2 data points around 4% close to 334 mbs (Bos, unpublished data); iron content by XRF meaurements (Lindström, S., communication); the isotopic composition of organic carbon (van de Schootbrugge *et al.*, 2018); the total amount of palynomorphs per gram sediment; the percentage of total spores that is aberrant (lower part by Bos (unpublished data)), the colour of the data point is determined by the most severely malformed palynomorph found in a sample; the total amount of heavy PAHs (m/z 228 and higher), corrected for TOC content in the sediment (lower interval by Grüters, 2012); and the Coronene / Benzo[a]pyren ratio (lower interval by Grüters, 2012).

25

5.4 PAHs pollution and mutagenesis

The chromatograms produced for PAH measurements on both types of GC-MS (e.g. figure 13 A) have peaks that are much wider compared to other studies (e.g. Naraoka *et al.*, 2000; Marynowski *et al.*, 2009; Grüters, 2012; Song *et al.*, 2020). There is no different preparation methodology which could have affected this, and therefore the reason for these wide peaks remains unknown.

Duplicate PAH measurements indicate that the method is rather precise, as most have similar total concentrations (figure 11) and a very similar distribution of PAH masses as the first round of measurements (figure 14). Of course, this does not have implications for the accuracy of the method. The total PAH concentrations of the duplicates are somewhat higher than those of the first round of measurements, where only the total concentration in sample Sch232.1 is significantly higher at the second run. This sample was measured on the Agilent GC-MS during the first measurement and on the DSQ GC-MS at the second measurement, while the other duplicate samples were run both times on the same GC-MS. However, the different machines should (theoretically) not affect the results, as all values are corrected for the response of the GC-MS using standards. As the chromatogram of the second run of Sch232.1 was quite difficult to integrate, the result might be slightly off. However, as the distribution of PAH masses are very identical between the two measurements (figure 14), this cannot explain the full difference in concentration.

Grüters (2012) measured two extreme high PAH concentrations around the TJB of the Schandelah-1 core, at 327.1 and 315.5 mbs. In those peaks, concentrations are at least 10 times higher than the rest of the section, and also many times higher compared to PAH concentrations around the TJB in other studies (e.g. van de Schootbrugge *et al.*, 2009; Pieñkowski *et al.*, 2010). Potentially, a piece of charcoal or other burned organic material has been measured in those two samples, creating these anomalously high values. Excluding these two spikes forms a better interpretable distribution pattern, and therefore these two measurements are not used in further comparison of my data to the TJB.

As discussed above, palynological results indicate that preservation of organic matter could have been lower within the red clay intervals. PAHs, being organic molecules, might also have been affected by the increase of oxidation, and it is possible that the trend in PAHs is caused by a lower preservation. However, PAHs are biochemical persistent molecules and have a low aqueous solubility (Johnsen *et al.*, 2005; Song *et al.*, 2020). It would thus be possible that PAHs were less affected by oxidation than other organic compounds. The potential for preserving molecular organic geochemical information can be assessed by studying the thermal maturity of a section (Song *et al.*, 2020). Thermal maturity would be a useful next step to assess the preservation of PAHs in the Schandelah-1 core.

Relative low PAH concentrations in the red intervals (figures 10 and 15) indicate no link to increased burning of organic matter, in contrast to what was hypothesised. In the interval between the red claystones, PAHs are present in higher concentrations, which potentially links to an increase in burning events. Comparing the PAH concentrations of the Upper Hettangian to the TJB (figure 16) indicates that between the red beds concentrations are relatively high, although they remain less than half of the maximum concentrations around the TJB. Interestingly, the earliest Sinemurian also contains relatively high concentrations, represented by the upper two samples. This is against expectations, as the Sinemurian is a rather stable period with little vegetational disturbances (figure 2; van der Weijst, 2015).

Within the Upper Hettangian, most PAHs have similar distribution patterns (figure 15), which, according to Jiang et al. (1998), suggests a common source. As most combustion-derived PAHs follow this trend, it could indicate a slight increas in combustion after the lowest red interval, around 251 mbs. Also Benzo(e)pyrene, the most stable 5-ring PAH (Stein, 1978; Nabbefeld et al., 2010) shows the highest values between the red intervals, mainly around 251 mbs. The same pattern is observed in the concentration of perylene, which is a biomarker for fungal organic matter. Possibly, fungal degradation was disturbed and less active during deposition of the red intervals, which is in line with the decrease in biodegradation as described by Hollaar (2017). Around the extinction interval, combustion-derived PAH concentrations are high in the second half of the ETE, directly preceding the TJB. As the increase of PAHs around the TJB is relatively close to depths with increased aberrant spores, it was seen as

a possibility that the carcinogenic PAHs are the cause of the mutagenic aberrant spores. However, the increase in PAHs occurs somewhat deeper in the core than the increase in aberrant spores. In the Upper Hettangian, with the low PAH concentrations in the red intervals, no link can be made between the mutagenesis and PAH pollution.

The ratio of Coronene to BaP could be used as an indicator for a source by forest fires (Freeman & Cattell, 1990; van de Schootbrugge et $al.$, 2009; Grüters, 2012). The Schandelah-1 core has high Cor/BaP values at the TJB, which indicates that a different PAHs source than wildfires is likely. CAMP volcanic activity and subsurface organic matter combustion is presented as a probable origin of the PAHs with this high ratio (Grüters, 2012). The data from this study also has a relatively high Cor/BaP ratio in the red intervals and at the start of the Sinemurian (figure 16), which is related to the slightly higher coronene concentrations relative to other PAH masses shown in figure 14. This could thus indicate a different source than forest fires in the red intervals as well, but due to the low sampling resolution and especially the low concentration of PAHs in the red claystones, no hard conclusion on the volcanic origin in the red intervals should be drawn. The increase in weathering and reworking witnessed in the red intervals could have washed older volcanic PAHs into the shallow marine sediments, interfering with the results. However, we would then expect to find higher concentrations of PAHs at these depths instead of the very low concentrations observed, which provides no indication for high amounts of reworked PAHs. Thus, it is likely that the PAHs in the red intervals and Sinemurian have different sources than wildfires, but whether this source would be subsurface coal burning induced by late CAMP volcanic pulses, cannot be concluded. In between the red intervals the Cor/BaP ratio is low, so a source from forest fires would be more likely in these intervals. However, the meaning of the Cor/BaP ratio has been doubted lately, as forest fires can reach higher temperatures than previously expected.

Could there be stress on the ecosystem caused by volcanism, without PAH indicating increased burning events? CAMP volcanic pulses started (201.635 $\pm$ 0.029 Ma) right before the beginning of the extinction event (201.564 $\pm$0.015 Ma), and continued to occur for 600,000 years (Marzoli et $al.$, 2011; Blackburn et al., 2013; Heimdal et $al.$, 2018). Due to this long period of volcanism, it can thus be expected that high PAH concentrations can be found for longer periods in the Early Hettangian. However, the few measurements in the lowest Jurassic show low PAH concentrations, with the exception of the concentration at 310 mbs of the Lower Hettangian (figure 16; Grüters, 2012). The PAH concentrations thus do not show long-term burning events in the Early Hettangian, although more data points in the lower Jurassic would be useful. However, we must consider that the TJB in the Schandelah-1 core could be bound by a hiatus, as abrupt changes are present in the S/P ratio, carbon isotopes and TOC concentrations. Therefore, we might miss part of the earliest Hettangian PAH concentrations and their potential link to CAMP induced biomass burning. The question remains how much time would be missing, and if this would cover the whole period of CAMP volcanism. If not, CAMP volcanism would have occurred in the Early Jurassic while PAH concentrations where rather low. This would question the use of PAHs are a proxy for volcanism.

Evidence for wildfires is based on the occurrence of elevated PAH concentrations, but can also be determined by the presence of charcoal fragments (Marynowski & Simoneit, 2009). Charcoal fragments have been observed in multiple palynology slides, but have not been counted. Studying charcoal abundance, sizes and shapes throughout the studied interval could provide more detailed indications for wildfires. In addition, a study into inertinite reflectance may be useful as it can indicate burning temperatures.

To obtain more conclusive results, PAH concentrations should be measured in higher resolution. For further measurements it would also be useful to include the m/z 202, as this will include the combustion derived pyrene and fluoranthene. These two are the only combustion derived PAHs that are excluded using the current method. Another useful next step would be to compare the mercury concentration to the PAH results and aberrant spore abundances. This could indicate whether the PAHs have a volcanic source and provide more conclusive information on the nature of terrestrial mutagenesis, as mercury is a highly toxic heavy metal. Unfortunately the mercury concentrations have not been measured yet, thus this comparison cannot be made at this moment.

5.5 Hettangian regular alternations

Based on the S/P record from the whole Hettangian, four individual fern spikes can be observed, of which the red intervals coincide with the last two (figure 2; van der Weijst, 2015). The same pattern is observed in the TOC content and δ $^{13}C_{org}$ records, although less obvious. Van der Weijst (2015) has applied spectral analysis on multiple Hettangian to Early Sinemurian proxy records (magnetic susceptibility, δ $^{13}C_{org}$ and S/P ratio) from the Schandelah-1 core. An average thickness between 21.4 and 26.7 meter per cycle is observed. The data from this study (S/P ratio, aberrant spores, palynomorph abundance, reworking and PAH concentrations) clearly fit the trend of this previously observed regular alternation. A comparison to a selection of this data is shown in figure 17. These regular alternations could potentially be astronomically forced by the stable 405 ky eccentricity cycle, which seems to fit the duration of the Hettangian period (201.5 to 199.5 Ma). If this were the case, this implies that astronomically driven climatic variations caused severe stress on Hettangian ecosystems which resulted in high amounts of aberrant spores. The results of the SEG model do indicate potential climatic variations on the scale of the red intervals, with a slightly dryer climate within the intervals than the rest of the section. Possible ways how the weak 405 kyr eccentricity cycle could have influenced the Hettangian climate are due to increased aridity, resulting in soil destabilisation and the increased erosion that is observed; or by long-term ozone depletion after the ETE which was more harmful to life with increased insolation, resulting in increased UV-radiation causing the high amounts of aberrant spores (comparable to Marshall *et al.*, 2020). In this case, it can be expected that the amount of aberrant spores would also be high during the lower two fern spikes of the Hettangian. The lowest of these two fern spikes fall within the last few measurements of the aberrant record in the earliest Hettangian (figure 16). These aberrant concentrations are higher than background conditions, but less high than the red intervals. Further research into aberrant forms throughout the Lower Hettangian is required to confirm whether astronomically driven fluctuations could have induced mutagenesis through climate forcing.

Environmental fluctuations are not observed for the Sinemurian. An explanation could be that the Hettangian had vulnerable, weak and unstable ecosystems in the aftermath of CAMP volcanism, and thus astronomically forced climate change affected the Hettangian strongly, causing severe stress on terrestrial vegetation. In the Sinemurian, ecosystems could have become more stable and strong, and could have anticipated better to climatic changes. The potential ozone depletion could have been replenished. As most records indicate that the upper red interval was less severe than the lower red interval (e.g. less aberrant spores with a lower severity, weaker positive carbon isotope excursion, less reworking), it might indeed indicate that the system was slowly moving toward the stability of the Sinemurian. More studies on astronomical climate forcing by the 405 kyr eccentricity cycle on unstable and recovering ecosystems should be done to confirm the ideas presented in this paragraph.

The perturbations of the Upper Hettangian could thus indicate astronomical climatic disturbance rather than late pulses of CAMP volcanic emplacement. However, without further studies on other volcanic proxies, such as mercury concentrations, a volcanic source cannot be excluded.
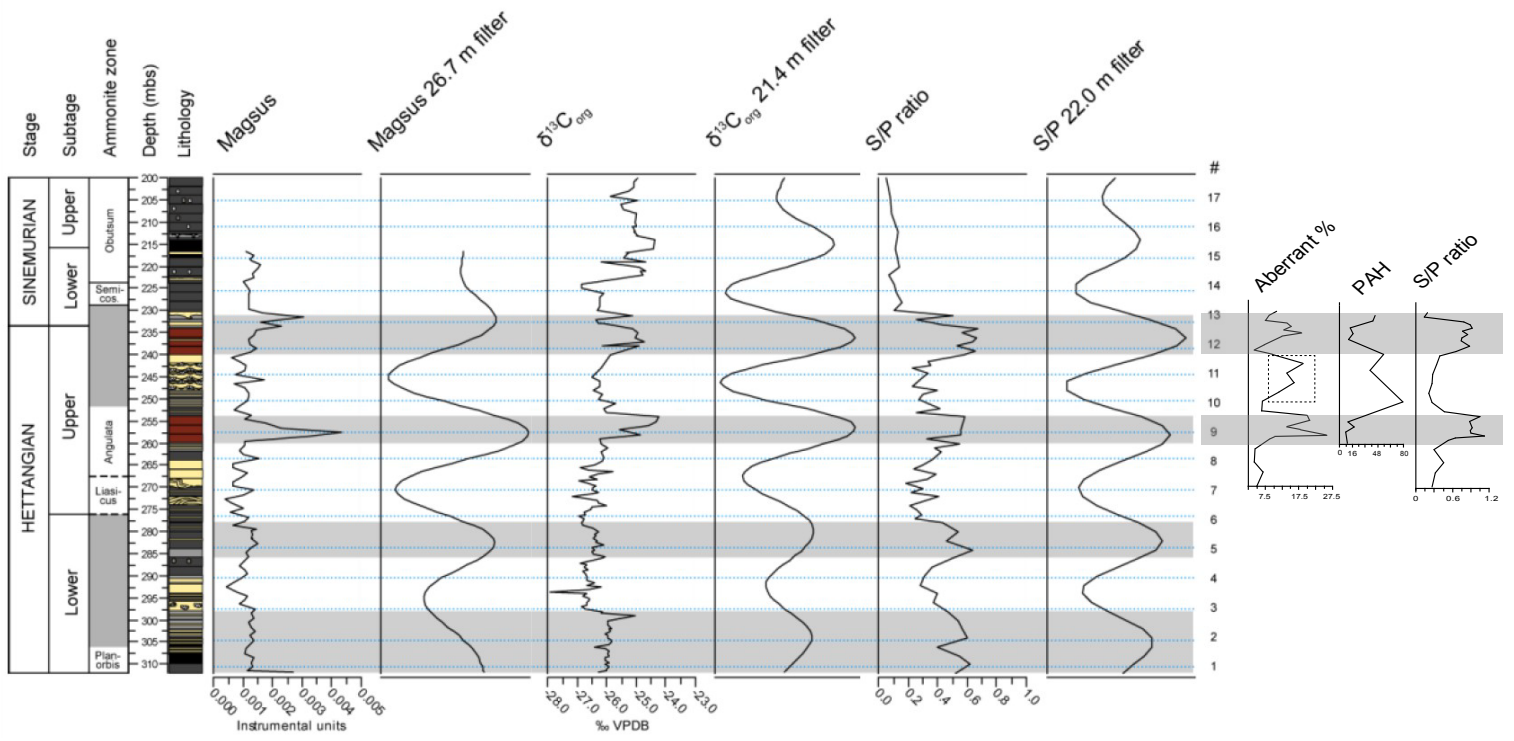
Figure 17: Comparison of the long period found by van der Weijst (2015) and a selection of data from the Upper Hettangian.

6   Conclusion

To conclude, there is clear evidence for highly stressed terrestrial ecosystems during the deposition of the red clay intervals of the Upper Hettangian. High degrees of mutagenic aberrant spores have been found close to and in these intervals. Extensive environmental disturbances and toxicity are needed to explain these high amounts of mutagenesis. Late pulses of CAMP volcanism have been proposed as cause of the environmental disturbances. Carcinogenic, combustion-derived polycyclic aromatic hydrocarbons were hypothesised to be (one of) the toxic substance responsible for the high amounts aberrant spores, as high degrees of PAHs have been found around the TJB relatively close to depths with increased amounts of aberrant spores. However, extreme low PAH concentrations have been found at the red clay beds, decoupling the mutagenesis from PAH pollution. Nonetheless, a volcanic source cannot be excluded, as lower amounts of PAHs could have been preserved in the red clay intervals, and it might be possible that volcanism occurred with low PAH emissions. A study in the mercury content should provide more information on the source of mutagenesis and the presence of volcanism.

The red clay intervals are characterized by low preservation, low biodegradation, high reworking and high amounts of spores, which all indicate soil instability, higher degrees of erosion and thus unstable terrestrial ecosystems. The lower preservation in these intervals could have removed part of the deposited PAHs and palynomorphs, and might have altered the organic carbon isotope signal. The SEG model results show a slightly dryer climate, which could have enhanced soil loss. Furthermore, the two red intervals both coincide to long regular alternations, which can be linked to the 405 kyr eccentricity cycle. Therefore it is proposed that the vegetation dynamics in the Hettangian can be the result of astronomical climate forcing on the recovering Hettangian ecosystems. This climate forcing might have increased aridity and soil erosion, or could have enhanced UV-radiation with increased insolation on a depleted ozone layer after the CAMP eruptions. Further studies are required to understand if and how astronomically forced climatic variations on the unstable Hettangian ecosystems could have caused such high degrees of aberrant spores.

7   Acknowledgements

8   References

1. Abbink, O. A. (1998). Palynological investigations in the Jurassic of the North Sea region. Laboratory of Palaeobotany and Palynology, Contributions Series 8. LPP Foundation Utrecht, 1- 191.

2. Abbink, O. A., Van Konijnenburg-Van Cittert, J. H. A., & Visscher, H. (2004). A sporomorph ecogroup model for the Northwest European Jurassic-Lower Cretaceousi: concepts and framework. Netherlands Journal of Geosciences, 83(1), 17-31.

3. Azevedo, R., Rodriguez, E., Mendes, R. J., Mariz-Ponte, N., Sario, S., Lopes, J. C., ... & Santos, C. (2018). Inorganic Hg toxicity in plants: A comparison of different genotoxic parameters. Plant Physiology and Biochemistry, 125, 247-254.

4. Bartolini, A., Guex, J., Spangenberg, J. E., Schoene, B., Taylor, D. G., Schaltegger, U., & Atudorei, V. (2012). Disentangling the Hettangian carbon isotope record: Implications for the aftermath of the end-Triassic mass extinction. Geochemistry, Geophysics, Geosystems, 13(1).

5. Beerling, D. J., & Berner, R. A. (2002). Biogeochemical constraints on the Triassic-Jurassic boundary carbon cycle event. Global Biogeochemical Cycles, 16(3), 10-1.

6. Benca, J. P., Duijnstee, I. A., & Looy, C. V. (2018). UV-B–induced forest sterility: Implications of ozone shield failure in Earth's largest extinction. Science advances, 4(2), e1700618.

7. Blackburn, T. J., Olsen, P. E., Bowring, S. A., McLean, N. M., Kent, D. V., Puffer, J., ... & Et-Touhami, M. (2013). Zircon U-Pb geochronology links the end-Triassic extinction with the Central Atlantic Magmatic Province. Science, 340(6135), 941-945.

8. Blakey, R. (2012). Paleogeography of Europe series. Colorado Plateau Geosystems, Inc. Downloaded from: https://deeptimemaps.com/

9. Bond, D. P., & Grasby, S. E. (2017). On the causes of mass extinctions. Palaeogeography, Palaeoclimatology, Palaeoecology, 478, 3-29.

10. Bonis, N. R., & Kürschner, W. M. (2012). Vegetation history, diversity patterns, and climate change across the Triassic/Jurassic boundary. Paleobiology, 38(2), 240-264.

11. Bos, R. (2020, March). *Long-term phytotoxicity and mutagenesis in terrestrial vegetation following the Triassic-Jurassic boundary.* Poster presented at the Nederlands Aardwetenschappelijk Congres (NAC), Utrecht.

12. Canfield, D. E. (1993). Organic matter oxidation in marine sediments. In Interactions of C, N, P and S biogeochemical Cycles and Global Change. Springer, Berlin, Heidelberg, 333-363.

13. Chandler, M. A., Rind, D., & Ruedy, R. (1992). Pangaean climate during the Early Jurassic: GCM simulations and the sedimentary record of paleoclimate. Geological Society of America Bulletin, 104(5), 543-559.

14. Deenen, M. H., Ruhl, M., Bonis, N. R., Krijgsman, W., Kuerschner, W. M., Reitsma, M., & Van Bergen, M. J. (2010). A new chronology for the end-Triassic mass extinction. Earth and Planetary Science Letters, 291(1-4), 113-125.

15. Flügel, E., & Kiessling, W. (2002). Patterns of Phanerozoic reef crises. Society for sedimentary geology, 72, 691-733.

16. Fowell, S. J., & Olsen, P. E. (1993). Time calibration of Triassic/Jurassic microfloral turnover, eastern North America. Tectonophysics, 222(3-4), 361-369.

17. Freeman, D. J., & Cattell, F. C. (1990). Woodburning as a source of atmospheric polycyclic aromatic hydrocarbons. Environmental Science & Technology, 24(10), 1581-1585.

18. Gradstein, F. M., Ogg, J. G., Schmitz, M., & Ogg, G. (Eds.). (2012). The geologic time scale 2012. Newsletters on stratigraphy, 45(2), 171-188.

19. Grice, K., Nabbefeld, B., & Maslen, E. (2007). Source and significance of selected polycyclic aromatic hydrocarbons in sediments (Hovea-3 well, Perth Basin, Western Australia) spanning the Permian–Triassic boundary. Organic Geochemistry, 38(11), 1795-1803.

20. Grime, J. P. (1977). Evidence for the existence of three primary strategies in plants and its relevance to ecological and evolutionary theory. The American Naturalist, 111(982), 1169-1194.

21. Grüters, J. (November 2012). Quellenzuordnung der polyzyklischen aromatischen Kohlenwasserstoffe (PAK) an der Trias/Jura-Grenze im Profil Schandelah (unpublished Master's thesis). Goethe Universität Frankfurt am Main, Germany.

22. Hallam, A. (1996). Recovery of the marine fauna in Europe after the end-Triassic and early Toarcian mass extinctions. Geological Society, London, Special Publications, 102(1), 231-236.

23. Hallam, A., & Wignall, P. B. (1997). Mass extinctions and their aftermath. Oxford University Press, UK.

24. Hallam, A., & Wignall, P. B. (1999). Mass extinctions and sea-level changes. Earth-Science Reviews, 48(4), 217-250.

25. Heimdal, T. H., Svensen, H. H., Ramezani, J., Iyer, K., Pereira, E., Rodrigues, R., ... & Callegaro, S. (2018). Large-scale sill emplacement in Brazil as a trigger for the end-Triassic crisis. Scientific reports, 8(1), 141.

26. Heunisch, C., Luppold, F. W., Reinhardt, L., & Röhling, H. G. (2010). Palynofazies, Bio- und Lithostratigrafie im Grenzbereich Trias/Jura in der Bohrung Mariental 1 (Lappwaldmulde, Ostniedersachsen)[Palynofacies, bio-and lithostratigraphy at the Triassic/Jurassic boundary in the Mariental 1 borehole (Lappwald Syncline, Eastern Lower Saxony.]. Zeitschrift der Deutschen Gesellschaft für Geowissenschaften, 161(1), 51-98.

27. Hochuli, P. A., Schneebeli-Hermann, E., Mangerud, G., & Bucher, H. (2017). Evidence for atmospheric pollution across the Permian-Triassic transition. Geology, 45(12), 1123-1126.

28. Huynh, T. T., & Poulsen, C. J. (2005). Rising atmospheric CO2 as a possible trigger for the end-Triassic mass extinction. Palaeogeography, Palaeoclimatology, Palaeoecology, 217(3-4), 223-242.

29. Jiang, C., Alexander, R., Kagi, R. I., & Murray, A. P. (1998). Polycyclic aromatic hydrocarbons in ancient sediments and their relationships to palaeoclimate. Organic Geochemistry, 29(5-7), 1721-1735.

30. Johnsen, A. R., Wick, L. Y., & Harms, H. (2005). Principles of microbial PAH-degradation in soil. Environmental pollution, 133(1), 71-84.

31. Larsson, L. M. (2009). Palynostratigraphy of the Triassic–Jurassic transition in southern Sweden. GFF, 131(1-2), 147-163.

32. Lindström, S., & Erlström, M. (2006). The late Rhaetian transgression in southern Sweden: Regional (and global) recognition and relation to the Triassic–Jurassic boundary. Palaeogeography, Palaeoclimatology, Palaeoecology, 241(3-4), 339-372.

33. Lindström, S., Pedersen, G. K., Van De Schootbrugge, B., Hansen, K. H., Kuhlmann, N., Thein, J., ... & Weibel, R. (2015). Intense and widespread seismicity during the end-Triassic mass extinction due to emplacement of a large igneous province. Geology, 43(5), 387-390.

34. Lindström, S. (2016). Palynofloral patterns of terrestrial ecosystem change during the end-Triassic event–a review. Geological Magazine, 153(2), 223-251.

35. Lindström, S., Sanei, H., Van De Schootbrugge, B., Pedersen, G. K., Lesher, C. E., Tegner, C., ... & Outridge, P. M. (2019). Volcanic mercury and mutagenesis in land plants during the end-Triassic mass extinction. Science advances, 5(10), eaaw4018.

36. Lindström, S., van de Schootbrugge, B., Hansen, K. H., Pedersen, G. K., Alsen, P., Thibault, N., ... & Nielsen, L. H. (2017). A new correlation of Triassic–Jurassic boundary successions in NW Europe, Nevada and Peru, and the Central Atlantic Magmatic Province: A time-line for the end-Triassic mass extinction. Palaeogeography, Palaeoclimatology, Palaeoecology, 478, 80-102.

37. Maliszewska-Kordybach, B. (1999). Persistent organic contaminants in the environment: PAHs as a case study. In Bioavailability of organic xenobiotics in the environment, Springer, Dordrecht. 3-34.

38. Marshall, J. E., Lakin, J., Troth, I., & Wallace-Johnson, S. M. (2020). UV-B radiation was the Devonian-Carboniferous boundary terrestrial extinction kill mechanism. Science Advances, 6(22), eaba0768.

39. Marynowski, L., & Simoneit, B. R. (2009). Widespread Upper Triassic to Lower Jurassic wildfire records from Poland: evidence from charcoal and pyrolytic polycyclic aromatic hydrocarbons. Palaios, 24(12), 785-798.

40. Marzoli, A., Bertrand, H., Knight, K. B., Cirilli, S., Buratti, N., Vérati, C., ... & Allenbach, K. (2004). Synchrony of the Central Atlantic magmatic province and the Triassic-Jurassic boundary climatic and biotic crisis. Geology, 32(11), 973-976.

41. Marzoli, A., Callegaro, S., Dal Corso, J., Davies, J. H., Chiaradia, M., Youbi, N., ... & Jourdan, F. (2018). The Central Atlantic magmatic province (CAMP): a review. In The Late Triassic World. Springer, Cham. 91-125.

42. Marzoli, A., Jourdan, F., Puffer, J. H., Cuppone, T., Tanner, L. H., Weems, R. E., ... & De Min, A. (2011). Timing and duration of the Central Atlantic magmatic province in the Newark and Culpeper basins, eastern USA. Lithos, 122(3-4), 175-188.

43. McElwain, J. C., Beerling, D. J., & Woodward, F. I. (1999). Fossil plants and global warming at the Triassic-Jurassic boundary. Science, 285(5432), 1386-1390.

44. McGhee Jr, G. R., Clapham, M. E., Sheehan, P. M., Bottjer, D. J., & Droser, M. L. (2013). A new ecological-severity ranking of major Phanerozoic biodiversity crises. Palaeogeography, Palaeoclimatology, Palaeoecology, 370, 260-270.

45. McHone, J. G. (2003). Volatile emissions from Central Atlantic Magmatic Province basalts: Mass assumptions and environmental consequences. Geophysical Monograph - American Geophyicial Union, 136, 241-254.

46. Mehlqvist, K., Vajda, V., & Larsson, L. M. (2009). A Jurassic (Pliensbachian) flora from Bornholm, Denmark–a study of a historic plant-fossil collection at Lund University, Sweden. GFF, 131(1-2), 137-146.

47. Menzie, C. A., Potocki, B. B., & Santodonato, J. (1992). Exposure to carcinogenic PAHs in the environment. Environmental science & technology, 26(7), 1278-1284.

48. Murchison, D. G., & Raymond, A. C. (1989). Igneous activity and organic maturation in the Midland Valley of Scotland. International Journal of Coal Geology, 14(1-2), 47-82.

49. Nabbefeld, B., Grice, K., Summons, R. E., Hays, L. E., & Cao, C. (2010). Significance of polycyclic aromatic hydrocarbons (PAHs) in Permian/Triassic boundary sections. Applied Geochemistry, 25(9), 1374-1382.

50. Nagajyoti, P. C., Lee, K. D., & Sreekanth, T. V. M. (2010). Heavy metals, occurrence and toxicity for plants: a review. Environmental chemistry letters, 8(3), 199-216.

51. Naraoka, H., Shimoyama, A., & Harada, K. (2000). Isotopic evidence from an Antarctic carbonaceous chondrite for two reaction pathways of extraterrestrial PAH formation. Earth and Planetary Science Letters, 184(1), 1-7.

52. Olsen, P. E., Shubin, N. H., & Anders, M. H. (1987). New Early Jurassic tetrapod assemblages constrain Triassic-Jurassic tetrapod extinction event. Science, 237(4818), 1025-1029.

53. Pieñkowski, G. (2004). The epicontinental Lower Jurassic of Poland. Polish Geological Institute Special Papers, 12, 1-154.

54. Pieñkowski, G., Niedzwiedzki, G., & Waksmundzka, M. (2012). Sedimentological, palynological and geochemical studies of the terrestrial Triassic–Jurassic boundary in northwestern Poland. Geological Magazine, 149(2), 308-332.

55. Quan, T. M., van de Schootbrugge, B., Field, M. P., Rosenthal, Y., & Falkowski, P. G. (2008). Nitrogen isotope and trace metal analyses from the Mingolsheim core (Germany): Evidence for redox variations across the Triassic-Jurassic boundary. Global Biogeochemical Cycles, 22(2).

56. Ruhl, M., Deenen, M. H. L., Abels, H. A., Bonis, N. R., Krijgsman, W., & Kürschner, W. M. (2010). Astronomical constraints on the duration of the early Jurassic Hettangian stage and recovery rates following the end-Triassic mass extinction (St Audrie's Bay/East Quantoxhead, UK). Earth and Planetary Science Letters, 295(1-2), 262-276.

57. Ruiz-Martínez, V. C., Torsvik, T. H., van Hinsbergen, D. J., & Gaina, C. (2012). Earth at 200 Ma: Global palaeogeography refined from CAMP palaeomagnetic data. Earth and Planetary Science Letters, 331, 67-79.

58. Sanei, H., Grasby, S. E., & Beauchamp, B. (2012). Latest Permian mercury anomalies. Geology, 40(1), 63-66.

59. Schaltegger, U., Guex, J., Bartolini, A., Schoene, B., & Ovtcharova, M. (2008). Precise U–Pb age constraints for end-Triassic mass extinction, its correlation to volcanism and Hettangian post-extinction recovery. Earth and Planetary Science Letters, 267(1-2), 266-275.

60. Schoene, B., Guex, J., Bartolini, A., Schaltegger, U., & Blackburn, T. J. (2010). Correlating the end-Triassic mass extinction and flood basalt volcanism at the 100 ka level. Geology, 38(5), 387-390.

61. Song, Y., Algeo, T. J., Wu, W., Luo, G., Li, L., Wang, Y., & Xie, S. (2019). Distribution of pyrolytic PAHs across the Triassic-Jurassic boundary in the Sichuan Basin, southwestern China: Evidence of wildfire outside the Central Atlantic Magmatic Province. Earth-Science Reviews, 102970.

62. Stein, S. (1978). On the high temperature chemical equilibria of polycyclic aromatic hydrocarbons. The Journal of Physical Chemistry, 82(5), 566-571.

63. Van de Schootbrugge, B., Payne, J. L., Tomasovych, A., Pross, J., Fiebig, J., Benbrahim, M., ... & Quan, T. M. (2008). Carbon cycle perturbation and stabilization in the wake of the Triassic-Jurassic boundary mass-extinction event. Geochemistry, Geophysics, Geosystems, 9(4).

64. Van de Schootbrugge, B., Quan, T. M., Lindström, S., Puttmann, W., Heunisch, C., Pross, J., ... & Rosenthal, Y. (2009). Floral changes across the Triassic/Jurassic boundary linked to ood basalt volcanism. Nature Geoscience, 2(8), 589-594

65. Van de Schootbrugge, B., Richoz, S., Pross, J., Luppold, F. W., Hunze, S., Wonik, T., ... & Fraguas, A. (2018). The Schandelah Scientific Drilling Project: A 25-million year record of Early Jurassic palaeo-environmental change from northern Germany. Newsletters on Stratigraphy. 52(3), 249-296.

66. Van de Schootbrugge, B., van der Weijst, C. M. H., Hollaar, T. P., Vecoli, M., Strother, P. K., Kuhlmann, N., ... & Lindström, S. (in review). Catastrophic soil loss associated with end-Triassic deforestation.

67. Van de Schootbrugge, B., & Wignall, P. B. (2016). A tale of two extinctions: converging end-Permian and end-Triassic scenarios. Geological Magazine, 153(2), 332-354.

68. Visscher, H., Looy, C. V., Collinson, M. E., Brinkhuis, H., Van Konijnenburg-Van Cittert, J. H., Kürschner, W. M., & Sephton, M. A. (2004). Environmental mutagenesis during the end-Permian ecological crisis. Proceedings of the National Academy of Sciences, 101(35), 12952-12956.

69. Von Hillebrandt, A. V., Krystyn, L., & Kuerschner, W. M. (2007). A candidate GSSP for the base of the Jurassic in the Northern Calcareous Alps (Kuhjoch section, Karwendel Mountains, Tyrol, Austria). International Subcommission on Jurassic Stratigraphy Newsletter, 34(1), 2-20.

70. Van der Weijst, C. M. H. (March 2015). Controls on vegetation dynamics in the wake of the end-Triassic mass extinction event (unpublished Master's thesis). Utrecht University, the Netherlands.

71. Whiteside, J. H., Olsen, P. E., Eglinton, T., Brookfield, M. E., & Sambrotto, R. N. (2010). Compound-specic carbon isotopes from Earth's largest flood basalt eruptions directly linked to the end-Triassic mass extinction. Proceedings of the National Academy of Sciences, 107(15), 6721-6725.

72. Wignall, P. B., & Bond, D. P. (2008). The end-Triassic and Early Jurassic mass extinction records in the British Isles. Proceedings of the Geologists Association, 119(1), 73-84.

9 Appendix

Table 1: Concentration of the total PAH and all isomers, all given in μg/g TOC. Depth is in mbs. PAH tot. = total PAH (sum of all isomers, also used in figures 11 and 16); Dupl. = duplicate measurement of the total PAHs; B[a]a = Benzo[a]anthracene; Chry = Chrysene or Triphenylene; 3.4-di = 3.4-dihydrocyclopenta(cd)pyrene; B[k]f = Benzo[k]fluoranthene; B[e]f = Benzo[e]fluoranthene; B[e]p = Benzo(e)pyrene; B[a]p = Benzo[a]pyrene; Pery = Perylene; Indeno = Indeno[1,2,3-c,d]pyrene; B[ghi]p = Benzo[ghi]perylene; Cor = Coronene.

Depth	PAH tot.	Dupl.	B[a]a	Chry	3.4-di	B[k]f	B[e]f	B[e]p	B[a]p	Pery	Indeno	B[ghi]p	Cor
232.1	44.72	89.01	0.54	0.18	0.00	2.58	0.00	1.15	1.86	3.94	22.45	0.38	11.64
233.3	41.91		0.27	0.38	0.53	3.14	0.00	1.24	1.82	3.06	1.74	21.82	7.91
234.8	13.59		1.57	0.01	0.00	2.38	0.00	0.63	1.50	0.30	0.32	3.40	3.48
236.1	16.79	19.97	0.18	1.73	0.00	0.74	2.97	0.54	2.08	0.00	1.18	3.31	4.08
237.4	11.21		1.24	0.09	0.00	2.22	0.43	0.45	0.58	0.31	0.29	3.09	2.50
240.7	55.26		1.00	4.13	0.00	4.49	0.52	3.14	6.27	5.88	3.17	18.69	7.97
244.2	38.02		0.91	3.39	0.00	2.74	0.50	2.09	5.02	4.75	2.18	11.65	4.79
251.2	79.12	87.50	0.10	6.49	0.00	6.20	10.34	9.87	0.00	0.00	4.70	30.74	10.68
255.6	10.71	19.97	0.72	0.00	0.00	2.14	1.62	0.00	0.00	0.00	0.44	2.76	3.02
256.7	18.70		1.73	0.17	0.00	4.72	0.00	0.69	1.07	0.32	0.78	4.66	4.56
257.8	7.86		0.66	0.05	0.01	1.70	0.00	0.76	0.15	0.00	0.17	2.30	2.06
260.3	9.74		0.12	0.80	0.00	0.93	0.27	0.95	0.98	0.00	0.69	3.46	1.55

Table 2: All counted palynomorphs. The sample depth in mbs is listed in the first row. The last 5 rows indicate reworked pollen, reworked spores, undetermined palynomorphs, the total aberrant spores and the amount of zircons found in a sample ('x' means no zircons were counted).

Palynomorphs	232	232.9	233.9	234.5	235.2	235.9	236.6	237.3	237.9	239.1	240.2	241.1	243	245	247	249	251	253	254	255	256.3	257	257.5	258.1	258.5	259	261	263.8	265.9	268.9
unidentified	47	25	13	25	23	22	18	19	14	13	24	28	20	38	11	28	36	50	42	12	41	13	41	41	20	32	40	43	38	74
SPORES																														
Spores indet	9	2	13	20	14	12	13	15	8	14	16	13	14	8	7	17	22	20	24	16	18	19	18	11	24	14	18	12	12	10
Acanthotriletes varius			4	11	14	11	15	8	8	8	1	14	3	3	3	2	22	13	3	3	6	2	4	1	3	1	1	1	2	1
Anapiculatisporites spiniger		1	1	2			1	1		1	1		2		3	2			1	3		2	2	2	3	1	1	1	1	
Aratrisporites minimus		1	1	1	1	1		2		1			1	1					1	2	1	1	3	3				1	1	1
Aratrisporites pilosus									1				1						1				1	1						
Aulisporites				4	1	1	1	2												1	1	1								
Baculatisporites comaumensis	4			3	5	5	5	3	5		1	4	1	1	1		2	7	2	4	2	5	7	2	2			1	2	2
Calamospora sp.	1	2	4	1	1	1	1	3	3	3	2	2		2	1		1	5	4	1			3	1	2	1	5	5	2	3
Camarozonosporites laevigatus																														
Ceratosporites spp.		1					1																							
Cingulizonates rhaeticus	1													1		1		1	1	2		1	2	1	1					
Cingulizonates spp.	2		3	1	1		2	2	5																					1
Concavisporites juvensis																														1
Concavisporites spp.	10	8	19	37	22	29	42	23	15	38	14	19	19	10	8	5	8	9	23	29	32	16	29	36	33	17	6	9	9	11
Contignisporites sp.		3	3	3	4	3	1	2	2	3	1		1	1	1		1		1	1		1	1	1	1					
Convolutisporites										1	1																			
Deltoidospora open trilete / broken	5	2	2	4	3	3	2	4	2	2	2	4	3	4	3	3	5	11	3	3	11	1	5	1	13	4	3	6	14	x
Deltoidospora sp.	42	9	38	39	34	30	38	43	28	40	34	27	29	21	26	16	25	43	48	60	58	58	57	37	25	24	32	20	14	10
Densosporites fissus				1			1	1				1				1		1				1	1	4		4				
Enzonalasporites						1	1										2	2			1					2	2			
Foveosporites																														
Inaguispora laevigata		2	2	1		1		1	1	1										1			1	1	1	1				2
Kraeuselisporites reissingerii	1		5		1	1	1			1	1	2			1					1				1	1					2
Laevigatosporites spp.						1															1								1	
Leiotriletes spp.			1	1	1	1		1	1											1		1								
Limbosporites lundbladii								1				1						1			1			1	1					
Lycopodiacidites sp.																		1												
Lycospora salebrosaceae				2	1	1		3	3	1		1	1	1				3	1		1	1	1	1						
Matonisporites crassiangulatus																			1		1		1							
Neoraistrickia spp.																						1	1							
Perinosporites thuringiacus																			1											
Polycingulizonates spp.																														
Polypodiisporites ipsviciensis				1			1		1																					
Polypodiisporites polymicrofoatus				1					1										1							1				
Punctatisporites spp.	3		3	1	4	2	4	1	2	2	1	2	1	1	3			4	6	1	2		2	2	1	2	2	1	1	1
Retitriletes austroclavidites												1																		
Retitriletes sp.																												1		
Stereisporites spp.				1	1	1	1		4		1	1		1	1		1	1	1		2				1	1	1	1		
Striatella spp.																		1	1									1		
Tigrisporites spp.												1																	1	
Todisporites spp.											1																			
Trachysporites fuscus	14	8	26	14	26	25	19	25	15	22	37	13	5	11	1	12	28	15	8	15	19	20	20	11	18	18	12	20	14	16
Uvaesporites argentaeformis						2	2	1	1		1		1			1		1	1					1	1					
Verrucosisporites spp.																					1									
Zebrasporites interscriptus																														
Zebrasporites laevigatus		1																												

Palynomorphs

Palynomorphs	268.9	265.9	263.8	261	259	258.5	258.1	257.5	257	256.3	255	254	253	251	249	247	245	243	241.1	240.2	239.1	237.9	237.3	236.6	235.9	235.2	234.5	233.9	232.9	232
POLLEN																														
Pollen indet	13	20	36	32	28	24	28	27	27	24	30	31	30	51	29	23	27	34	31	22	20	26	14	21	15	23	24	18	25	51
Alisporites sp.				1													3	1								2			2	
Araucariacites australis	25	21	16	16		8	10	9	13	12	22	19	19	4	8	8	3	8	7	6	11	7	17	22	12	4	3	6	6	3
Bisaccates indet	18.5	25	29.5	27	32	21	14	24.5	30	11	16	23	23	17.5	15.5	14	28	36.5	19	18	30.5	23.5	31.5	26	23	26	34	28.5	37	29.5
Brachysaccus							1					1	1																	
Callialasporites		1																					1							
Cedripites																														
Cerebropollenites macroverrucosus													1																	
Cerebropollenites mesozoicus													1																	
Cerebropollenites thiergartii		3		6	1	5	9	2	9	6	10	10	1	4	7	7	1	11	10	10	3	3	4	3	3	5	6	4	8	13
Chasmatosporites apertus		2		1	1		1	1	2	1	2	4		2	1	1	1		2			1	1	1	1	1	5	6	4	1
Chasmatosporites elegans		1		1		1	1	1	1		2	2	1				1							1						
Chasmatosporites hians	2		3			2	2	1	2	2	1	1	2		1	1		2							2					
Chasmatosporites major	5	6	5	7		4	4	4		1		8	8	3	5	5	2	6	4	4		3	1	1	5	4	1	1	2	1
Classopollis	37	44	21	35	20	17	14	23	45	61	12	6	6	53	45	43	36	28	31	30	11	28	13	12	23	16	19	18	35	33
Cycadopithes		1				2				1	2	1	1		1	2	1	2	1		1	2					1	1		
Ephedripites																														
Eucommiidites sp.		1		1		2						2	2			1	1	1		3	1	3	2	1		1	4	4	1	
Granuloperculatipollis rudis																														
Lunatisporites rhaeticus							1																						1	
Ovalipollis ovalis																														
Ovalipollis pseudoalatus																														
Perinopollenites elatoides	133	99	80	105	93	86	46	59	29	70	34	28	68	109	129	123	125	80	103	87	57	73	63	54	80	47	50	81	131	111
Pinuspollenites minimus		1	1	1		1	2	1		1	1	2		4	5	3	5	4		6			3	3	1	1		1	1	
Platysaccus spp.																					1				1					
Podosporites																														
Quadraeculina anellaeformis	1	1	1			1	2	2		1	2	1	1		2		4	4		1		1	1	3	6	4	1		2	5
Rhaetipollis germanicus			1																3											
Ricciisporites tuberculatus	6		6		1	3	7	2	16		4	11		1	1	1	1	6	1	3	3	3		2	4	5	3	3	3	2
Spheripollenites						1													2	2		1		1	1		1			
Sulcate pollen indet	1			1	1	3	1	3	7	4	3	5	5	1	2	2	2	1	3	7	7	7	7	5		3	2	2	6	1
Tsugaepollenites pseudomassulae	1		1	1		2		1			1			1				1	1		1				1					
MARINE																														
Acritach indet		1						1																						
Baltisphaeridium indet	1	1												1			1		1					1				1	1	
Baltisphaeridium spp.																														1
Cymatiosphaera sp.											1	1	1	1		1	1	1			1									
Dapcodinium priscum	3		1						1		1			1	2	1	1	1	1	2				1		1		7	7	11
Dinoflagellate indet	3											3			3			3											1	1
Leiosphaeridia						1			2							1								1						1
Micrhystridium	3			1		3					1			1	6				1	5	3	5		5	1		2	3	6	2
Prasinophytes indet	2		3	3		3		7	1	1	6	8	1	6	5	10	10			3	2	1		5	2	1	2		3	2
Tytthodiscus									1			1																		
foraminifera	1			1							1	2	2		1		2						1		1		1			
Schizocystia																														
Botryococcus	3	2	5	10		1	1	1	1	1		4	2			1								1		1			1	
Reworked pollen	1	1		1		5	1		4	2	1	2	4		1		1			3		1	1	1		2			2	
Reworked spores	3			1		8	8	1	6	1	5	3	3	2	2	2	2	1	3			1	5	5	2	2	3	3	3	3
Reworked palynomorph				1					2				1			1							1	1					1	1
Total aberrant spores	3	4	4	3	8	36	29	24	19	28	30	5	6	3	10	13	8	5	10	10	15	15	25	4	21	20	10	15		
Zircons	x	x	x	x	x	x	x	x	x	x	x	x	x	x	x	x	x	x	18	23	1	0	x	x	x	4	8	15	40	6

Table 3: The division of palynomorphs in ecogroups. N.A: not attributable. B/F/L: brackish, freshwater and lagoonal.

Ecogroup	Pollen	Spore	Marine
Reworked	*Lunatisporites rhaeticus*	*Cingulizonates spp.*	
	Ovalipollis ovalis	*Cingulizonates rhaeticus*	
	Ovalipollis pseudoalatus	*Aulisporites*	
	Riccisporites tuberculatus		
Lowland - wet	*Perinopollenites elatoides*	*Leiotriletes spp.*	
		Laevigatosporites spp.	
		Concavisporites spp.	
		Concavisporites jurensis	
		Acanthotriletes varius	
Lowland - dry	*Chasmatosporites apertus*	*Iraquispora laevigata*	
	Chasmatosporites hians	*Contignisporites sp.*	
	Chasmatosporites major	*Deltoidospora spp.*	
	Chasmatosporites elegans	*Matonisporites crassiangulatus*	
	Cycadopithes		
	Eucommiidites sp.		
River		*Stereisporites spp.*	
		Calamospora spp.	
		Baculatisporites comaumensis	
		Punctatisporites spp.	
		Todisporites spp.	
		Neoraistrickia spp.	
		Verrucosisporites spp.	
		Uvaesporites argentaeformis	
Upland	*Bisaccates indet*		
	Pinuspollenites minimus		
	Alisporites sp.		
	Brachysaccus		
	Quadraeculina anellaeformis		
Coastal	*Araucariacites australis*	*Anapiculatisporites spiniger*	
	Callialasporites	*Aratrisporites pilosus*	
	Classopollis	*Aratrisporites minimus*	
	Platysaccus spp.	*Densosporites fissus*	
		Kraeuselisporites reissingerii	
Tidal		*Retitriletes austroclavidites*	
		Retitriletes sp.	
Pioneer	*Cerebropollenites mesozoicus*		
	Cerebropollenites macroverrucosus		
	Cerebropollenites thiergartii		

Ecogroup	Pollen	Spore	Marine
N.A	Pollen indet	Spores indet	
	Podosporites	Polycingulizonates spp.	
	Sulcate pollen indet	Polypodiisporites polymicroforatus	
	Cedripites	Polypodiisporites ipsviciensis	
	Ephedripites	Striatella spp.	
	Granuloperculatipollis rudis	Tigrisporites spp.	
	Rhaetipollis germanicus	Trachysporites fuscus	
	Tsugaepollenites pseudomassulae	Camarozonosporites laevigatus	
	Spheripollenites	Foveosporites	
		Limbosporites lundbladii	
		Lycopodiacidites sp.	
		Lycospora salebrosaceae	
		Zebrasporites interscriptus	
		Zebrasporites laevigatus	
		Ceratosporites spp.	
		Enzonalasporites	
		Perinosporites thuringiacus	
		Convolutispora	
Aquaric - marine			Dinoflagellate indet
			Dapcodinium priscum
			Micrhystridium
			Baltisphaeridium spp.
			Acritach indet
			foraminifera
Aquaric - b/f/l			Leiosphaeridia
			Prasinophytes indet
			Cymatiosphaera sp.
			Tytthodiscus
			Schizocystia
			Botryococcus
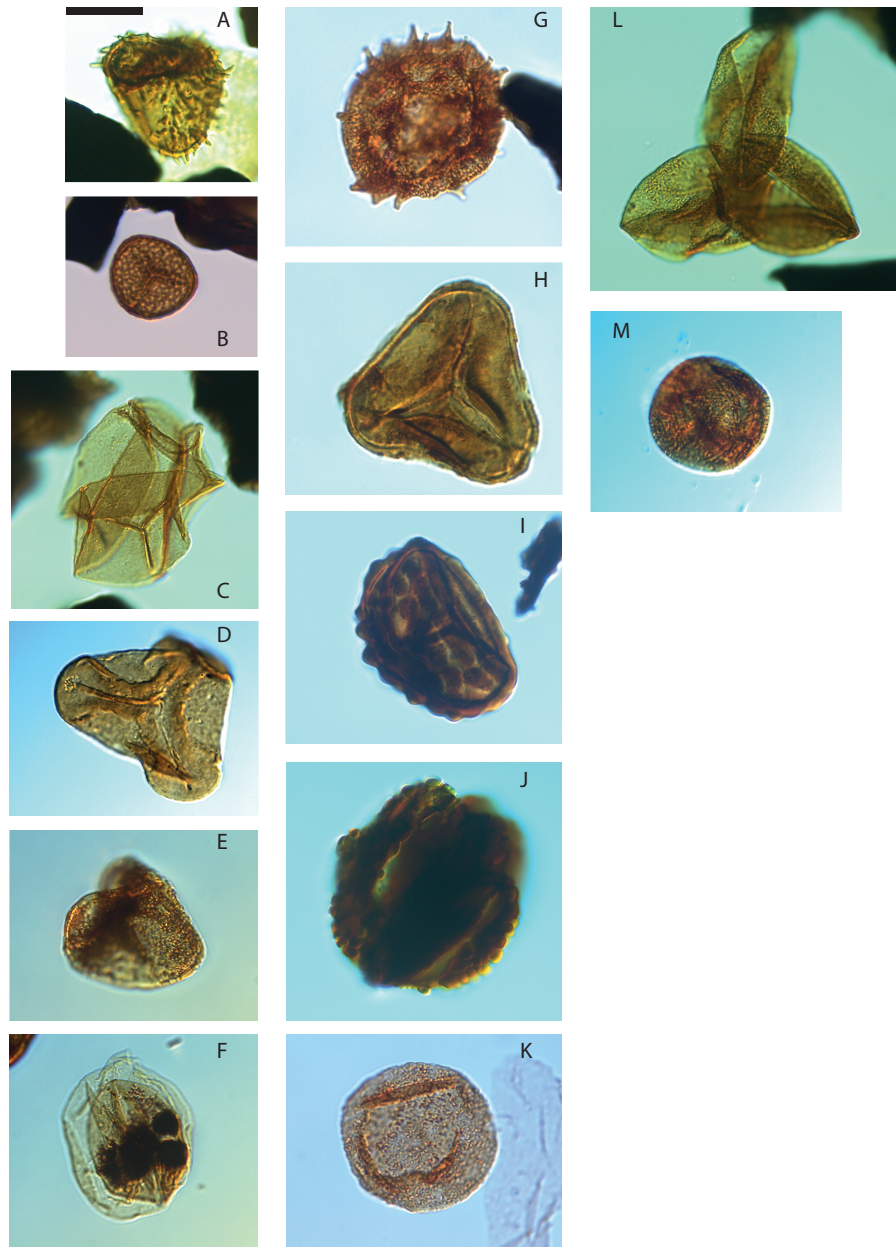
Plate 2. A selection of common palynomorphs of the Upper Hettangian. Scalebar = 20 μm. A. *Acanthotriletes varius*; B. *Stereisporites hauteriviensis*; C. *Calamospora* spp.; D. *Concavisporites* spp.; E. *Trachysporites fuscus*; F. *Perinopollenites elatoides*; G. *Kraeuselisporites reissingerii*; H. *Deltoidospora* spp.; I. *Contignisporites* spp.; J. *Ricciisporites tuberculatus* tetrad; K. *Araucariacites australis*; L. *Chasmatisporites major*, 3 attached; M. *Classopollis* spp.
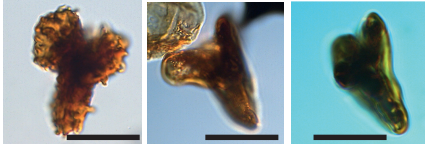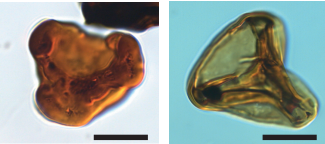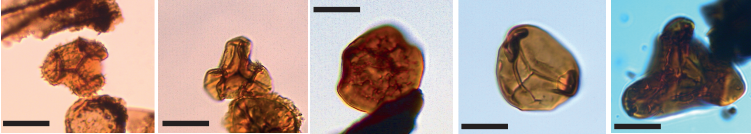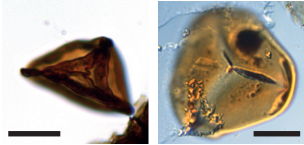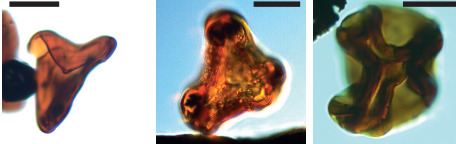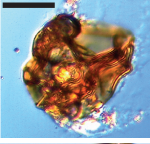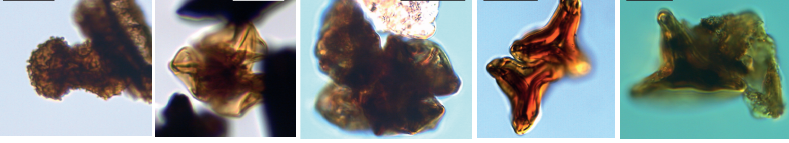
Teratology	Characteristics
Mild	Dwarfed and unexpanded
Mild to moderate	Thicker labra
	Cracks or folds
	Deformed or uneven length trilete rays
Moderate	Not 3 trilete rays, or indentations on spore margin
Moderate to severe	Wrinckled proximal area
	Not fully separated

Plate 3. Aberrant spores from the Upper Hettangian arranged after teratology category as defined by Lindström *et al.*, 2019. Scale bar = 20 μm.